

Fed-ADE: Adaptive Learning Rate for Federated Post-adaptation under Distribution Shift

Heewon Park^{1*}, Mugon Joe^{2*}, Miru Kim^{1*}, Kyungjin Im², Minhae Kwon^{1†}

¹ Department of Electrical and Computer Engineering, Sungkyunkwan University, Republic of Korea

² Soongsil University, Seoul, Republic of Korea

Abstract

Federated learning (FL) in post-deployment settings must adapt to non-stationary data streams across heterogeneous clients without access to ground-truth labels. A major challenge is learning rate selection under client-specific, time-varying distribution shifts, where fixed learning rates often lead to underfitting or divergence. We propose Fed-ADE (Federated Adaptation with Distribution Shift Estimation), an unsupervised federated adaptation framework that leverages lightweight estimators of distribution dynamics. Specifically, Fed-ADE employs uncertainty dynamics estimation to capture changes in predictive uncertainty and representation dynamics estimation to detect covariate-level feature drift, combining them into a per-client, per-timestep adaptive learning rate. We provide theoretical analyses showing that our dynamics estimation approximates the underlying distribution shift and yields dynamic regret and convergence guarantees. Experiments on image and text benchmarks under diverse distribution shifts (label and covariate) demonstrate consistent improvements over strong baselines. These results highlight that distribution shift-aware adaptation enables effective and robust federated post-adaptation under real-world non-stationarity. The code is available at <https://github.com/h2w1/Fed-ADE>

1. Introduction

Machine learning models are increasingly deployed across edge devices such as smartphones, IoT sensors, and autonomous systems, where each device continuously receives a non-stationary data stream [25, 46, 59, 60]. FL has emerged as a key paradigm to support such decentralized learning under privacy constraints, enabling model collaboration without raw data sharing [12, 21, 30, 31, 35, 36, 44, 51, 61]. In practice, models are pre-trained on centralized datasets and deployed to client devices, but their performance

often degrades quickly due to distribution shifts in the real-time data. These shifts appear in multiple forms, such as label distribution shift and covariate shift, and evolve in client-specific and heterogeneous ways [16, 20, 27, 28, 33, 43, 49].

This environment introduces two major sources of heterogeneity: (i) shift heterogeneity, where each client experiences different temporal dynamics of distribution shift [8, 20, 22, 27, 41, 43, 68], and (ii) data heterogeneity, where clients' local datasets already differ in scale, domain, or semantics [12, 36, 47, 51, 61]. Together, these factors make federated post-deployment adaptation highly challenging, as a single global model or fixed training learning rate is insufficient to cope with diverse and evolving conditions.

A critical yet underexplored aspect of this problem is the choice of learning rate. In online adaptation, learning rate selection directly governs both stability and responsiveness. Fixed learning rates fail to reflect data distribution shifts, leading to underfitting when the learning rate is too small, or divergence when the learning rate is too large [2, 3, 11, 42]. The difficulty is amplified in FL, where hundreds of heterogeneous clients undergo distinct, time-varying distribution shifts without access to ground-truth labels.

To address this, we propose Fed-ADE, a lightweight and unsupervised adaptation framework. Figure 1 shows the overview of the proposed Fed-ADE system. Fed-ADE introduces two estimators of distribution dynamics: *Uncertainty dynamics estimation*, which captures predictive uncertainty changes, and *representation dynamics estimation*, which detects embedding-level drift. By combining these signals, Fed-ADE assigns a per-client, per-timestep adaptive learning rate that reflects local distribution. Unlike prior approaches relying on multi-model ensembles or costly hyperparameter search, Fed-ADE requires no extra communication or supervision. Furthermore, we provide theoretical analyses showing that dynamics estimation approximates underlying distribution evolution and yields dynamic regret guarantees. Empirically, we validate Fed-ADE across image and text benchmarks under label and covariate shift environments, where it consistently improves adaptation accuracy and efficiency compared to strong baselines.

*Equal contribution.

†Corresponding author. minhae.kwon@skku.edu

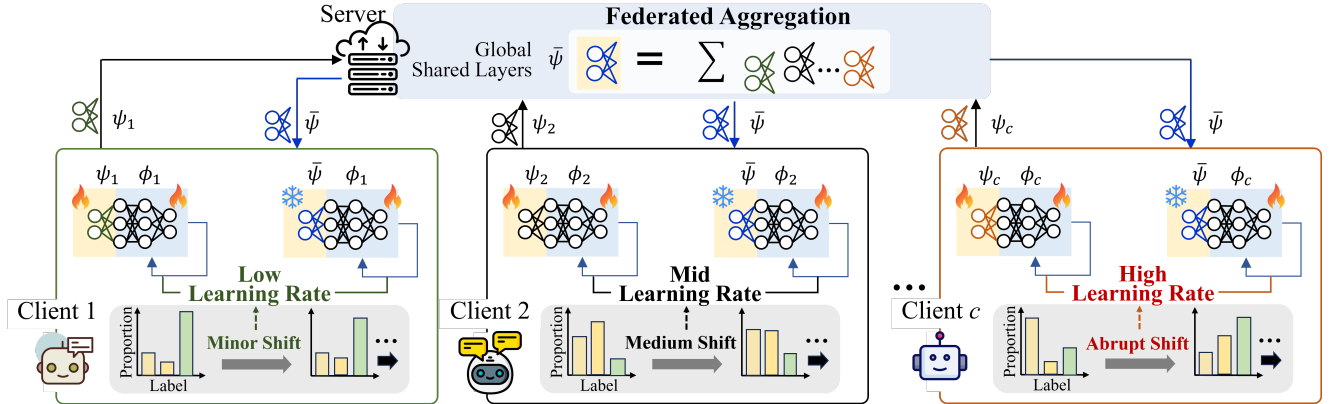


Figure 1. Overview of the Fed-ADE. Each client receives a pre-trained model, splits it into shared (ψ_c) and personalized (ϕ_c) layers, and adapts to unlabeled, distribution-shifting data using an adaptive learning rate.

In summary, our contributions are as follows.

- We propose Fed-ADE, a novel framework for unsupervised federated post-adaptation under heterogeneous and time-varying distribution shifts, addressing real-time data distribution shifts.
- We introduce two lightweight estimators: Uncertainty dynamics estimation, which captures predictive uncertainty changes, and representation dynamics estimation, which detects embedding-level drift. These estimators enable per-client, per-timestep adaptive learning rates without requiring ground-truth labels.
- We provide theoretical analyses showing that distribution shift estimation approximates true distribution shift and that the resulting learning dynamics satisfy dynamic regret bound and convergence guarantees.
- We conduct extensive experiments on four image and a text benchmarks under label and covariate shift, demonstrating that Fed-ADE consistently outperforms state-of-the-art baselines while remaining computationally efficient.

2. Related Works

Federated Learning for Decentralized Data Environments FL is a widely adopted framework for collaboratively training machine learning models across multiple decentralized clients while preserving data privacy [12, 23, 34, 35, 44, 61]. Early approaches such as FedAvg [44] proposed aggregating locally updated model parameters on a central server without sharing raw data. However, this paradigm encounters challenges caused by data heterogeneity, as each client may hold data drawn from distinct distributions [23, 34, 35]. To mitigate these issues, personalized FL methods have been introduced to better adapt models to the local characteristics of each client’s data. Among them, partial-sharing strategies train only a subset of layers collaboratively via FL, while the remaining layers are updated locally [12, 27, 51, 61]. These methods enhance personalization and local adaptation, yet they commonly assume

stationary or globally synchronized data distributions across clients. In contrast, our work introduces a novel system that supports post-deployment adaptation by employing an unsupervised, per-client adaptive learning rate mechanism, which dynamically adjusts to real-time distributional shifts.

Distribution Shift Adaptation Distribution shift arises in various forms, including label and covariate shift [13, 15, 26, 53, 55, 64]. Online label shift adaptation adjusts predictions without true labels, as in ATLAS [2] and FTH [58]. Covariate shift is commonly addressed by domain adaptation methods such as UDA [18] and UNIDA [63], which mainly assume centralized settings and are not readily applicable to federated or online scenarios. In federated environments, adaptation approaches such as Fed-POE [43], ATP [4], and FedSPL [38] mitigate client heterogeneity or adapt models to unlabeled target clients through ensemble strategies, adaptation-specific rules, or pseudo-labeling. However, these methods often introduce additional computational overhead or auxiliary components during adaptation.

3. Preliminaries

Pre-training ($t = 0$) Let θ be the global model trained at the server using pre-collected data $(\mathbf{x}_G^0, \mathbf{y}_G^0)$, where \mathbf{x}_G^0 follows feature distribution $\mathbf{Q}_{G,x}^0$ and \mathbf{y}_G^0 follows label distribution $\mathbf{Q}_{G,y}^0$. We also denote by $\mathbf{Q}_{G,x|y}^0$ the conditional distribution of features given labels, and by $\mathbf{Q}_{G,y|x}^0$ the conditional distribution of labels given features. Each label \mathbf{y}_G^0 is an index i , where i is an element of the class index set \mathcal{I} . In the distribution $\mathbf{Q}_{y_G^0}$, the i -th component, $[\mathbf{Q}_{y_G^0}]_i$, represents the proportion of class $i \in \mathcal{I}$ in the label set \mathbf{y}_G^0 .

Online Distribution Shift ($0 < t \leq T$) Consider a set of federated clients \mathcal{C} collaboratively performing post-deployment adaptation. Each client model θ_c is initialized from the pre-trained global model θ . At time t , client $c \in \mathcal{C}$ observes an unlabeled data stream \mathbf{x}_c^t drawn from a client and

time-dependent distribution $\mathbf{Q}_{c,x}^t$, while the corresponding labels \mathbf{y}_c^t follow $\mathbf{Q}_{c,y}^t$ but remain unobserved. For brevity, we use \mathbf{Q}_c^t to denote the overall data distribution at time t .

A temporal distribution shift occurs when $\mathbf{Q}_c^t \neq \mathbf{Q}_c^{t-1}$. Typical cases include: (1) label distribution shift, where $\mathbf{Q}_{c,y}^t$ changes while $\mathbf{Q}_{c,x|y}^t$ stays approximately stable and (2) covariate shift, where $\mathbf{Q}_{c,x|y}^t$ changes while $\mathbf{Q}_{c,y}^t$ is approximately constant. Following prior works [2, 58, 62], we model the shift of \mathbf{Q}_c^t as

$$\mathbf{Q}_c^t = (1 - \omega(t)) \mathbf{Q}_c^0 + \omega(t) \mathbf{Q}_c^T, \quad (1)$$

where $\omega(t) \in [0, 1]$ is a weighting function interpolating between the initial distribution \mathbf{Q}_c^0 and a later distribution \mathbf{Q}_c^T . In the federated setting, we assume that \mathbf{Q}_c^0 aligns with the pre-training data distribution, whereas \mathbf{Q}_c^T represents each client's distinct distribution evolved after deployment, reflecting client-specific environments and behaviors.

In this setting, an unsupervised federated post-adaptation framework is required to adjust to the continuously changing data distributions with limited client samples, while maintaining robust global performance.

Learning Objective with Unsupervised Risk Estimation

Under the federated setting with online distribution shift, each client $c \in \mathcal{C}$ aims to update its local model θ_c using only unlabeled data. We adopt an unsupervised risk estimation framework that enables model updates without access to ground-truth labels. Let the expected risk for client c at time t be defined as

$$\begin{aligned} \mathcal{F}_c^t(\theta_c) &\triangleq \mathbb{E}_{\mathbf{y}_c^t \sim \mathbf{Q}_{c,y}^t} \left[\mathcal{L}(\mathcal{H}(\theta_c; \mathbf{x}_c^t), \mathbf{y}_c^t) \right] \\ &= \sum_{i \in \mathcal{I}} [\mathbf{Q}_{c,y}^t]_i \cdot \mathcal{F}_c^{t,i}(\theta_c), \end{aligned} \quad (2)$$

where $\mathcal{H}(\cdot)$ denotes the softmax prediction of the model, $\mathcal{L}(\cdot)$ is the loss function, and $\mathcal{F}_c^{t,i}(\theta_c)$ is the class-wise risk for class i , which can be expressed as $\mathbb{E}_{\mathbf{y}_c^t \sim [\mathbf{Q}_{c,y}^t]_i} [\mathcal{L}(\mathcal{H}(\theta_c; \mathbf{x}_c^t), \mathbf{y}_c^t)]$. The expected risk can be decomposed as

$$\mathcal{F}_c^t(\theta_c) = \sum_{i \in \mathcal{I}} [\mathbf{Q}_{c,y}^t]_i \mathcal{F}_c^{0,i}(\theta_c), \quad (3)$$

where $\mathcal{F}_c^{0,i}(\theta_c)$ denotes the class-wise risk computed from the initial data $(\mathbf{x}_c^0, \mathbf{y}_c^0)$, which is assumed to follow the same distribution as the global pre-training data. Hence, $\mathcal{F}_c^{0,i}(\theta_c)$ can be approximated by its empirical counterpart $\widehat{\mathcal{F}}_c^{0,i}(\theta_c)$ using $(\mathbf{x}_c^0, \mathbf{y}_c^0)$.

Since labels are not observable during post-adaptation, the current label distribution $\mathbf{Q}_{c,y}^t$ must be estimated. We employ the Black-box Shift Estimation (BBSE) method [40] for this purpose, which corrects the pseudo-label distribution via $\mathbf{Q}_{c,y}^t \approx \mathbf{M}^{-1} \mathbf{Q}_{c,\hat{y}}^t$. Here, \mathbf{M} is a confusion matrix

computed on the server using pre-training data $(\mathbf{x}_G^0, \mathbf{y}_G^0)$ and shared with clients, while $\mathbf{Q}_{c,\hat{y}}^t$ denotes the prediction distribution over the unlabeled batch \mathbf{x}_c^t .¹ Using these estimates, the unsupervised risk can be approximated as

$$\widehat{\mathcal{F}}_c^t(\theta_c) = \sum_{i \in \mathcal{I}} \left[\widehat{\mathbf{M}}^{-1} \mathbf{Q}_{c,\hat{y}}^t \right]_i \cdot \widehat{\mathcal{F}}_c^{0,i}(\theta_c), \quad (4)$$

where $\widehat{\mathbf{M}}$ is empirical estimator of the confusion matrix.

Finally, the federated learning objective based on the estimated unsupervised risk in (4) is to jointly optimize all client models as follows.

$$\{\theta_c^*\}_{c=1}^C = \arg \min_{\theta_c} \sum_{c=1}^C \widehat{\mathcal{F}}_c^t(\theta_c) \quad (5)$$

Personalized Federated Learning with Layer Decoupling

To achieve the goal in (5) under heterogeneous client distributions (i.e., \mathbf{Q}_c^t may differ across c and shift over time), we adopt a partial-sharing FL method that decouples each client model θ_c into shared layers ψ_c and personalized layers ϕ_c , where only the shared layers ψ_c are communicated with the server while the personalized layers ϕ_c are retained locally [12, 27, 39, 47, 51, 61]. Specifically, we adopt two step local update method [12, 27, 51, 61]. Each client participates in R rounds of federated communication. In round $r \in \{1, \dots, R\}$, a subset of clients $\mathcal{C}^{(r)} \subset \mathcal{C}$ updates both shared and personalized layers locally with the learning rate η_c^t , and the risk estimator $\widehat{\mathcal{F}}_c^t(\{\psi_c, \phi_c\})$ obtained in (4) as follows.

$$\{\psi_c, \phi_c\} \leftarrow \{\psi_c, \phi_c\} - \eta_c^t \nabla_{\psi_c, \phi_c} \widehat{\mathcal{F}}_c^t(\{\psi_c, \phi_c\}) \quad (6)$$

Then, each clients sends ψ_c to the server, which aggregates them using a weighted average based on each client's local dataset size N_c^t as follows.

$$\bar{\psi} = \frac{1}{\sum_{c \in \mathcal{C}^{(r)}} N_c^t} \sum_{c \in \mathcal{C}^{(r)}} N_c^t \psi_c \quad (7)$$

The server broadcasts $\bar{\psi}$ to all clients, who set $\psi_c \leftarrow \bar{\psi}$ and thus hold $\theta_c = \{\bar{\psi}, \phi_c\}$. After receiving $\bar{\psi}$, clients freeze the shared layers and adapt only the personalized layers as follows.

$$\phi_c \leftarrow \phi_c - \eta_c^t \nabla_{\phi_c} \widehat{\mathcal{F}}_c^t(\{\bar{\psi}, \phi_c\}) \quad (8)$$

With this update strategy, clients can preserve aggregated global knowledge in $\bar{\psi}$ while capturing the client-specific structure in ϕ_c .

¹Details of BBSE and the derivation of the risk estimator are provided in Appendix B.

Algorithm 1 Fed-ADE

```
1: Inputs: Total rounds  $R$ , and learning rate bounds  
    $[\eta_{\min}, \eta_{\max}]$   
2: Initialize: Local model  $\{\psi_c, \phi_c\}$ , previous summaries  
    $(\mathbf{q}_c^{t-1}, \mathbf{z}_c^{t-1})$   
3: for  $r = 1, 2, \dots, R$  do  
4:   Server samples participants  $\mathcal{C}^{(r)} \subset \mathcal{C}$   
5:   for  $c \in \mathcal{C}^{(r)}$  in parallel do  
6:     Build unsupervised risk  $\widehat{\mathcal{F}}_c^t(\psi_c, \phi_c)$  as (4)  
7:     Compute batch summaries  $\mathbf{q}_c^t$  and  $\mathbf{z}_c^t$   
8:     Estimate dynamics  $\mathcal{S}_{\text{unc},c}^t$  as (12),  $\mathcal{S}_{\text{rep},c}^t$  as (14)  
9:     Combine shift dynamic signals  $\mathcal{S}_c^t$  as (10)  
10:    Set adaptive learning rate  $\eta_c^t$  as (9)  
11:    Update local model  $\{\psi_c, \phi_c\}$  by (6)  
12:    Send  $\psi_c$  to server  
13:  end for  
14:  Server aggregates to obtain  $\bar{\psi}$  via (7)  
15:  Server broadcasts  $\bar{\psi}$   
16:  for  $c \in \mathcal{C}^{(r)}$  in parallel do  
17:    Replace shared layers  $\psi_c \leftarrow \bar{\psi}$   
18:    Update personalized layers  $\phi_c$  as (8)  
19:    Cache  $(\mathbf{q}_c^{t-1}, \mathbf{z}_c^{t-1}) \leftarrow (\mathbf{q}_c^t, \mathbf{z}_c^t)$   
20:  end for  
21: end for
```

4. Distribution Shift Driven Federated Post-adaptation

In this section, we introduce Fed-ADE, a federated post-adaptation framework designed to address heterogeneous and time-varying distribution shifts across clients. Fed-ADE adaptively controls learning rates of each client based on the degree of local distribution shift, enabling fast yet stable post-deployment adaptation. The overall process of Fed-ADE is shown in Algorithm 1.

4.1. Distribution Shift Adaptive Learning Rate

The effectiveness of adaptation in (6) and (8) hinges on selecting a learning rate η_c^t that reflects how rapidly the local data distribution shifts at client c at timestep t . To capture this temporal shift, Fed-ADE introduces a distribution dynamics signal \mathcal{S}_c^t that quantifies the magnitude of the observed distribution shift. The learning rate is then adaptively scheduled according to this signal as follows.

$$\eta_c^t = \eta_{\min} + (\eta_{\max} - \eta_{\min}) \mathcal{S}_c^t \quad (9)$$

The adaptive rate η_c^t is bounded within $[\eta_{\min}, \eta_{\max}]$. A higher \mathcal{S}_c^t indicates stronger distribution shift, resulting in a larger η_c^t for faster adaptation, whereas a smaller \mathcal{S}_c^t implies stability, leading to a lower η_c^t for conservative updates. This mechanism allows Fed-ADE to automatically balance adaptivity and stability in real-time across heterogeneous

clients.

4.2. Distribution Shift Dynamics Signal

We next describe how the dynamics signal \mathcal{S}_c^t is constructed. At each timestep t , client c estimates the extent of its local distribution shift using two complementary components: (i) an uncertainty-based estimator $\mathcal{S}_{\text{unc}}^t$ that captures predictive uncertainty changes, and (ii) a representation-based estimator $\mathcal{S}_{\text{rep}}^t$ that measures embedding-level drift. These signals are combined to form a unified signal as follows.

$$\mathcal{S}_c^t = \frac{1}{2} (\mathcal{S}_{\text{unc}}^t + \mathcal{S}_{\text{rep}}^t) \in [0, 1] \quad (10)$$

Here, larger \mathcal{S}_c^t indicates stronger local drift, prompting a corresponding increase in the adaptive learning rate.

Uncertainty Dynamics Estimation To capture temporal changes in predictive uncertainty, each client summarizes its model outputs over the current data batch \mathbf{x}_c^t using the mean softmax vector as

$$\mathbf{q}_c^t = \frac{1}{|\mathbf{x}_c^t|} \sum_{x \in \mathbf{x}_c^t} \mathcal{H}(\{\psi_c, \phi_c\}; x), \quad (11)$$

where \mathbf{q}_c^t represents the aggregated predictive distribution. This serves as an entropy-based proxy for uncertainty, providing a label-free summary of class-level belief of the model. Batch-level averaging normalizes for batch size and mitigates per-sample stochasticity. The temporal change in predictive uncertainty is then measured via the cosine distance between consecutive batches as follows.

$$\mathcal{S}_{\text{unc}}^t = 1 - \cos(\mathbf{q}_c^{t-1}, \mathbf{q}_c^t) \in [0, 1] \quad (12)$$

This yields values in $[0, 1]$ since both \mathbf{q}_c^{t-1} and \mathbf{q}_c^t are normalized probability vectors. Smaller $\mathcal{S}_{\text{unc},c}^t$ indicates stable predictions with low uncertainty drift, whereas values closer to 1 reflect stronger predictive changes. Computation requires storing only \mathbf{q}_c^{t-1} , incurring $O(|\mathcal{I}|)$ memory overhead.

Representation Dynamics Estimation To capture shifts in the embedding space, Fed-ADE summarizes the feature representation as an ℓ_2 -normalized batch mean, which ensures that cosine distance reflects only directional changes rather than scale differences, as

$$\mathbf{z}_c^t = \frac{1}{|\mathbf{x}_c^t|} \sum_{x \in \mathbf{x}_c^t} \frac{h_{\psi_c}(x)}{\|h_{\psi_c}(x)\|_2} \in \mathbb{R}^d, \quad (13)$$

where $h_{\psi_c}(\cdot)$ denotes the feature extractor parameterized by ψ_c , and \mathbf{z}_c^t represents the batch-level latent feature vector.

The magnitude of the feature-level shift is then computed as follows.

$$\mathcal{S}_{\text{rep}}^t = \frac{1}{2}(1 - \cos(\mathbf{z}_c^{t-1}, \mathbf{z}_c^t)) \in [0, 1] \quad (14)$$

The scaling value $\frac{1}{2}$ normalizes the cosine distance from its natural range $[0, 2]$ to $[0, 1]$, aligning it with the uncertainty dynamics signal $\mathcal{S}_{\text{unc}}^t$. This estimator is fully label-free, operates locally, and only requires storing \mathbf{z}_c^{t-1} , incurring $O(d)$ memory overhead.

5. Theoretical Analyses

We provide theoretical analyses underpinning Fed-ADE. We first establish that the cumulative uncertainty and representation dynamics surrogates based on cosine similarity accurately approximate their respective true distribution shifts in unlabeled federated settings. These cumulative quantities are then used to derive a dynamic regret bound, in which each client's adaptive learning rate η_c^t is determined by its instantaneous combined shift signal \mathcal{S}_c^t , achieving the standard min-max optimal rate under non-stationarity. The analysis that verifies the adaptive updates in Fed-ADE satisfy convergence guarantees under non-stationary environments is provided in Appendix F.

5.1. Cumulative Shift Surrogates and Error Bounds

Cumulative Uncertainty Dynamics The true cumulative deviation of the predictive-distribution marginal $\sum_{t=1}^T \|\mathbf{Q}_{c,y}^t - \mathbf{Q}_{c,y}^{t-1}\|_1$ is unobservable in practice. We instead use the surrogate $\bar{\mathcal{S}}_{\text{unc}} \triangleq \sum_{t=1}^T \mathcal{S}_{\text{unc}}^t$. Under standard calibration, concentration, and non-degeneracy assumptions, $\bar{\mathcal{S}}_{\text{unc}}$ tracks the true predictive-distribution path length up to a small additive error.

Theorem 1 (Error Bound: Cumulative Uncertainty Dynamics). *Assume ϵ -calibration with respect to $\mathbf{Q}_{c,y}^t$, i.e., $\|\mathcal{H}(\{\psi_c, \phi_c\}; \mathbf{x}_c^t) - \mathbf{y}_c^t\|_2 \leq \epsilon_t$ in expectation. Then, the cumulative estimation error is bounded as*

$$\left| \bar{\mathcal{S}}_{\text{unc}} - \sum_{t=1}^T \|\mathbf{Q}_{c,y}^t - \mathbf{Q}_{c,y}^{t-1}\|_1 \right| \leq K_{\text{cos}} \sum_{t=2}^T (\epsilon_t + \epsilon_{t-1}), \quad (15)$$

where K_{cos} is the Lipschitz constant of the cosine similarity function.

Proof. See Appendix C. \square

Cumulative Representation Dynamics For representation-level drift, we define $\bar{\mathcal{S}}_{\text{rep}} \triangleq \sum_{t=1}^T \mathcal{S}_{\text{rep}}^t$. Under standard concentration of normalized feature means and the Lipschitz continuity of the shared layers h_{ψ_c} , which extract local representations, $\bar{\mathcal{S}}_{\text{rep}}$ accurately tracks the temporal evolution of local feature representations.

Theorem 2 (Error Bound: Cumulative Representation Dynamics). *Assume $\|\mathbf{z}_c^t - \bar{\mathbf{z}}_c^t\|_2 \leq \epsilon'_t$, where $\bar{\mathbf{z}}_c^t = \mathbb{E}[h_{\psi_c}(x)/\|h_{\psi_c}(x)\|_2]$, and that h_{ψ_c} is K_h -Lipschitz. Then, the cumulative estimation error is bounded as*

$$\left| \bar{\mathcal{S}}_{\text{rep}} - \sum_{t=1}^T \frac{1}{2} \left(1 - \frac{\langle \bar{\mathbf{z}}_c^{t-1}, \bar{\mathbf{z}}_c^t \rangle}{\|\bar{\mathbf{z}}_c^{t-1}\|_2 \|\bar{\mathbf{z}}_c^t\|_2} \right) \right| \leq K_h \sum_{t=2}^T (\epsilon'_t + \epsilon'_{t-1}), \quad (16)$$

where ϵ'_t denotes the feature-level approximation error.

Proof. See Appendix D. \square

Combined Cumulative Shift Surrogate We define the total cumulative shift surrogate as $\bar{\mathcal{S}}_c = \frac{1}{2}(\bar{\mathcal{S}}_{\text{unc}} + \bar{\mathcal{S}}_{\text{rep}})$. Let \mathcal{V}_c denote the corresponding combined true shift measure. Then, by Theorems 1 and 2, and applying the triangle inequality, we obtain the following.

$$|\bar{\mathcal{S}}_c - \mathcal{V}_c| \leq \frac{1}{2} \left[K_{\text{cos}} \sum_{t=2}^T (\epsilon_t + \epsilon_{t-1}) + K_h \sum_{t=2}^T (\epsilon'_t + \epsilon'_{t-1}) \right]$$

Hence, the combined surrogate $\bar{\mathcal{S}}_c$ closely tracks the true distribution shifts and can be directly used in the subsequent dynamic regret analysis.

5.2. Dynamic Regret Analyses

At each timestep t , client c updates its model parameters $\{\psi_c, \phi_c\}$ and incurs a loss $\mathcal{F}_c^t(\{\psi_c, \phi_c\}) = \mathcal{L}(\mathcal{H}(\{\psi_c, \phi_c\}, \mathbf{x}_c^t), \mathbf{y}_c^t)$. The *dynamic regret* over T rounds is defined as

$$\text{Reg}_T \triangleq \sum_{t=1}^T \mathcal{F}_c^t(\{\psi_c, \phi_c\}) - \sum_{t=1}^T \min_{\{\psi_c^t, \phi_c^t\}} \mathcal{F}_c^t(\{\psi_c, \phi_c\}),$$

where $\min_{\{\psi_c^t, \phi_c^t\}} \mathcal{F}_c^t$ denotes the instantaneous optimal loss at each round. This formulation quantifies the additional cost incurred by non-stationarity in the local data distribution.

Dynamic Regret Bound Prior analyses of online distribution shift [7, 48, 52] provide an $\mathcal{O}(\sqrt{T})$ *static regret* bound against a fixed comparator. In contrast, in non-stationary environments where client data distributions evolve over time, we establish a *dynamic regret* bound that scales with the cumulative shift proxy $\bar{\mathcal{S}}_c$.

Let $G \triangleq \sup_{(\mathbf{x}_c^t, \mathbf{y}_c^t)} \|\nabla_{\{\psi_c, \phi_c\}} \mathcal{L}(\mathcal{H}(\{\psi_c, \phi_c\}, \mathbf{x}_c^t), \mathbf{y}_c^t)\|_2$ be an upper bound on the gradient norm, and $B \triangleq \sup_{(\mathbf{x}_c^t, \mathbf{y}_c^t)} |\mathcal{L}(\mathcal{H}(\{\psi_c, \phi_c\}, \mathbf{x}_c^t), \mathbf{y}_c^t)|$ an upper bound on the loss value. Under the assumptions of Lemma 5 (Appendix B), running gradient descent with a constant learning rate η yields the following result.

Theorem 3 (Dynamic Regret Bound). *Let Reg_T denote the dynamic regret over T rounds. Let $\sigma > 0$ be the minimum singular value of the confusion matrix \mathbf{M} , Γ a projection constant, and $|\mathcal{I}|$ the number of classes. Then, for learning rate η , the expected regret satisfies*

$$\begin{aligned} \mathbb{E}[\text{Reg}_T] &\leq 2 \left(\frac{|\mathcal{I}|G^2}{\sigma^2} + B^2 \right) \eta T + \frac{\Gamma^2}{\eta} + \frac{4(\Gamma + 1)\sqrt{B\bar{S}_c T}}{\eta} \\ &\approx \mathcal{O} \left(\eta T + \frac{1}{\eta} + \frac{\sqrt{\bar{S}_c T}}{\eta} \right). \end{aligned} \quad (17)$$

Proof. See Appendix E. \square

The three terms ηT , $1/\eta$, and $\sqrt{\bar{S}_c T}/\eta$ correspond to optimization error, projection cost, and adaptation cost due to distributional shifts, respectively. By tuning the learning rate η with respect to \bar{S}_c , Fed-ADE achieves the min–max optimal dynamic regret rate under non-stationarity.

Min–max Optimality Fed-ADE employs the adaptive learning rate rule (9), parameterized by $[\eta_{\min}, \eta_{\max}]$, where \bar{S}_c^t denotes the instantaneous shift signal at round t . Choosing η_{\min} and η_{\max} such that $\eta_{\min} \leq \eta^* \leq \eta_{\max}$, with $\eta^* = \Theta(T^{-1/3}\bar{S}_c^{1/3})$ being the theoretically optimal rate, ensures that η_c^t remains within the valid range. This choice satisfies the convergence conditions in Theorem 12 and guarantees that Theorem 3 attains min–max optimality as follows.

$$\mathbb{E}[\text{Reg}_T] = \mathcal{O} \left(\bar{S}_c^{\frac{1}{3}} T^{\frac{2}{3}} \right). \quad (18)$$

Further description for min-max optimality is provided in Appendix E.2.

Remark 4. The regret rate $\mathcal{O}(\bar{S}_c^{1/3} T^{2/3})$ achieved by Fed-ADE matches the min–max optimal bound for non-stationary online learning under unsupervised label shift [5]. The adaptive rate bound $[\eta_{\min}, \eta_{\max}]$ is designed to contain the optimal value estimated by \bar{S}_c , aligning theoretical guarantees with practical adaptivity in dynamic federated environments.

6. Simulation Results

In this section, we conduct extensive experiments to validate the effectiveness of the proposed methods. We first briefly introduce the simulation setups and then present numerical results on various datasets. The detailed description of the simulation setups is provided in Appendix G, and results of extra simulations are provided in Appendix H.

6.1. Simulation Settings

Shift Scenarios and Datasets We evaluate Fed-ADE across three prototypical online distribution-shift settings—label shift and covariate shift—using standard image

benchmarks (Tiny ImageNet [32], CIFAR-10 [29], CIFAR-100 [29], CIFAR-10-C [19], CIFAR-100-C [19]) and the text benchmark LAMA [50].

- **Label shift** is simulated by gradually changing each client’s class prior over time, following one of four temporal schedules (linear (Lin.), sine (Sin.), square (Squ.), Bernoulli (Ber.) on Tiny ImageNet [32], CIFAR-10 [29], and LAMA [50] benchmarks.
- **Covariate shift** is modeled using corruption benchmarks CIFAR10-C [19] and CIFAR100-C [19], where clients observe progressively changing corruption severity levels following one of four temporal schedules (Lin., Sin., Squ., Ber.).

Baselines for Comparing Adaptation Methods We compare the proposed Fed-ADE with the following baselines.

- **Localized Learning:** We evaluate four centralized unsupervised online adaptation methods—FTH [58], ATLAS [2], UNIDA [63], and UDA [18]. These methods perform adaptation locally without any client collaboration, thus lacking the ability to leverage shared knowledge across users.
- **Federated Learning:** We evaluate two federated adaptation methods—Fed-POE [43], and FedCCFA [9] that combine locally fine-tuned models with aggregated global models over time, using a fixed learning rate irrespective of shift magnitude.
- **Fed-ADE (fixed learning rate):** We evaluate fixed learning rate (FixLR) variants that remove adaptivity from Fed-ADE and use constant stepsizes within the same bounds as Fed-ADE; For image benchmarks, we use 5×10^{-6} for FixLR(Low), 10^{-5} for FixLR(Mid), and 10^{-4} for FixLR(High). For LAMA, we use 10^{-4} for FixLR(Low), 10^{-3} for FixLR(Mid), and 10^{-2} for FixLR(High).
- **Fed-ADE (ours):** Our method performs personalized federated post-adaptation by dynamically adjusting the local learning rate based on estimated distribution-shift magnitude. For all image benchmarks, we set $\eta_{\min} = 5 \times 10^{-6}$ and $\eta_{\max} = 10^{-4}$, while for the text-based LAMA benchmark we use $\eta_{\min} = 10^{-3}$ and $\eta_{\max} = 10^{-2}$.

Evaluation Protocols At each timestep, clients adapt using unlabeled data and are evaluated on the same data with labels, reporting accuracy averaged over clients and timesteps. We assume clients do not know the pre-training distribution and initialize with uniform priors. For simulation, We set the total number of timesteps to 100 and the total number of clients to 100.

6.2. Simulation Results

Performance of Adaptation Methods Table 1 summarizes the results across three prototypical shift scenarios—label and covariate—over diverse datasets. Overall,

Table 1. Performance comparison of different online adaptation methods (average accuracy (%) and average wall time (sec.))

Dataset	Shift	Localized Learning				Federated Learning					
		FTH	ATLAS	UNIDA	UDA	Fed-POE	FedCCFA	FixLR(Low)	FixLR(Mid)	FixLR(High)	Fed-ADE
(i) Label Shift Scenarios											
Tiny ImageNet	Lin.	78.2±1.0	76.5±1.3	83.8±0.1	74.5±0.2	87.1±0.2	84.7±0.8	87.5±1.2	88.2±1.1	86.1±0.4	89.1±0.1
	Sin.	77.9±0.8	76.8±1.1	83.2±0.5	74.5±0.2	87.5±0.4	84.8±0.7	87.3±1.4	88.0±1.1	87.6±0.6	88.9±0.1
	Squ.	77.2±0.8	78.5±1.4	83.3±0.1	74.7±0.3	86.4±0.9	83.0±0.9	87.4±1.2	88.2±0.7	86.4±0.5	88.9±0.1
	Ber.	78.2±1.1	77.6±1.1	82.7±0.3	73.8±0.8	86.5±0.7	83.8±0.9	86.5±1.7	87.8±1.2	86.3±0.6	88.7±0.1
CIFAR-10	Lin.	31.4±0.8	36.5±4.3	23.0±0.3	33.3±1.4	71.3±3.2	65.8±0.5	70.6±2.0	70.8±2.1	63.8±1.9	73.8±0.6
	Sin.	40.3±0.9	43.7±5.1	22.9±0.3	32.0±1.3	71.4±2.6	65.8±0.8	69.4±1.5	70.5±1.6	64.3±2.2	73.6±0.5
	Squ.	31.7±0.7	32.3±5.0	23.1±0.1	28.1±1.4	70.6±1.9	65.3±0.3	72.8±2.1	71.6±2.0	70.6±2.5	72.2±1.6
	Ber.	30.6±0.9	32.7±5.9	23.0±0.1	28.5±1.5	69.6±1.5	65.4±0.4	68.3±1.7	71.8±1.6	70.0±2.2	72.9±2.2
LAMA	Lin.	68.3±1.2	79.5±3.2	31.2±0.8	72.9±2.0	85.4±1.3	95.6±0.1	86.7±1.2	95.2±2.0	24.6±3.3	95.8±0.4
	Sin.	74.7±3.1	71.8±5.0	31.1±0.6	70.6±6.8	84.0±1.6	91.6±0.9	88.0±0.8	94.7±2.4	26.9±4.1	95.8±0.6
	Squ.	70.5±6.5	79.8±0.9	31.2±0.5	74.4±0.2	84.2±1.0	92.0±0.1	88.6±0.2	95.4±1.2	26.9±5.3	96.4±0.6
	Ber.	76.8±0.2	78.0±5.8	31.1±0.5	70.9±6.5	84.1±0.6	91.1±0.5	87.9±0.3	94.3±2.4	20.0±4.7	95.9±0.5
(ii) Covariate Shift Scenarios											
CIFAR-10 CIFAR-10-C	Lin.	23.7±0.2	13.9±0.2	43.3±0.6	45.7±0.8	44.5±0.8	43.1±0.5	63.4±0.2	63.9±0.3	40.6±2.1	64.4±0.2
	Sin.	22.9±0.2	13.2±0.2	44.8±0.1	43.5±0.3	44.7±1.2	43.3±0.4	63.5±0.3	63.7±0.3	38.1±3.1	64.8±0.1
	Squ.	23.8±0.1	14.1±0.4	42.2±0.1	43.3±0.2	48.5±1.2	41.6±0.7	62.7±2.1	64.5±2.1	39.6±2.8	65.4±0.2
	Ber.	23.6±0.2	14.2±0.3	42.7±0.2	42.3±0.1	48.7±0.9	42.0±0.5	64.1±2.1	64.4±2.1	40.8±2.2	65.8±0.2
CIFAR-100 CIFAR-100-C	Lin.	9.2±0.1	3.5±0.1	34.3±0.1	35.6±0.2	27.3±0.1	24.3±0.3	44.0±0.2	43.4±0.6	41.4±0.6	45.8±0.2
	Sin.	7.6±0.2	2.9±0.1	34.1±0.1	35.7±0.1	27.5±0.1	24.5±0.5	43.9±0.1	42.1±0.2	39.8±0.3	46.7±0.1
	Squ.	8.5±0.1	3.4±0.1	33.8±0.2	35.3±0.1	31.9±0.1	25.1±0.4	44.9±0.3	42.8±0.2	34.3±0.5	46.5±0.3
	Ber.	8.6±0.1	3.5±0.1	33.0±0.1	34.7±0.2	31.3±0.1	25.2±0.4	45.3±0.5	43.5±0.2	31.1±0.4	46.8±0.1
Average Wall Time		2631.2±71.3	1959.2±22.6	1886.5±3.7	1242.7±7.8	130.7±1.9	210.8±16.6	109.5±0.4	109.5±0.4	109.5±0.4	109.5±0.4

Fed-ADE achieves the highest accuracy in all settings while maintaining the lowest wall-clock time. Localized adaptation methods (FTH, ATLAS, UNIDA, UDA) exhibit limited robustness and incur substantially higher computation, whereas federated approaches such as Fed-POE and FedCCFA provide improved stability but still fall short of Fed-ADE in dynamic environments.

Under label distribution shift, Fed-ADE consistently surpasses all baselines across all temporal schedules (Lin., Sin., Squ., Ber.). On Tiny ImageNet and CIFAR-10, Fed-ADE provides steady improvements over FixLR and Fed-POE, with average gains of about 1% and 4%, respectively. A similar pattern is observed on the text-based LAMA benchmark: despite its larger label space and noisier dynamics, Fed-ADE still maintains the highest accuracy across all temporal schedules, improving over the best federated baselines by roughly 2% on average.

In covariate shift scenarios, centralized domain adaptation methods (UDA, UNIDA) struggle in the federated setting, showing notably low robustness across all corruption severities. Fed-ADE consistently surpasses both FixLR and Fed-POE, achieving an average improvement rate of roughly 3% over FixLR and more than 6% over Fed-POE.

In terms of computational cost, Fed-ADE delivers superior performance with exceptional efficiency. Its average wall time (≈ 109 sec) is 17–24 \times faster than localized meth-

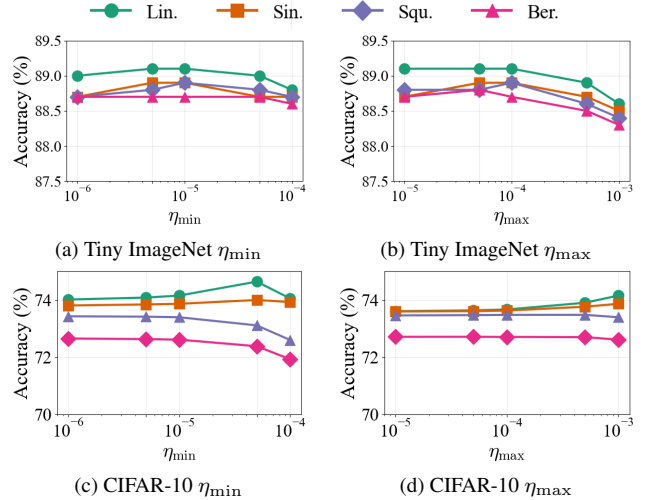


Figure 2. Impact of learning rate bounds on Fed-ADE under label shift scenarios on Tiny-ImageNet and CIFAR-10 datasets.

ods and roughly 2 \times faster than FedCCFA, despite achieving consistently higher accuracy. These results indicate that Fed-ADE provides both accuracy and scalability under diverse online distribution shifts, achieving dynamic robustness without sacrificing computational efficiency—unlike existing approaches that specialize in only one shift type or incur substantial overhead.

Table 2. Performance with Pre-trained Model Trained on Various Distributions with CIFAR-10.

Distribution Shift	Fed-ADE	FedCCFA	Fed-POE	UDA	UNIDA	ATLAS	FTH	
Gaussian	Lin.	69.2±1.7	62.3±1.2	65.7±2.1	20.1±2.0	20.2±1.8	25.3±2.2	22.3±1.7
	Sin.	68.3±1.6	63.1±1.5	64.8±1.7	27.8±2.4	27.7±2.2	33.5±2.3	23.9±2.1
	Squ.	66.4±1.5	61.9±2.6	61.4±2.2	20.3±2.1	19.8±1.7	23.1±2.0	23.0±1.8
	Ber.	67.1±1.3	63.0±2.5	60.9±2.5	18.2±2.3	17.7±1.9	22.5±2.1	21.6±1.9
Exponential Decay	Lin.	67.4±1.6	54.1±3.3	61.1±1.8	23.4±3.1	25.4±2.8	26.1±1.5	22.3±1.9
	Sin.	67.6±1.6	54.2±2.5	61.4±2.5	23.9±2.9	24.5±2.3	25.6±2.1	21.5±1.7
	Squ.	66.9±1.5	52.3±3.2	55.3±2.7	19.2±4.3	21.7±2.0	26.6±2.2	21.4±1.7
	Ber.	66.7±1.1	53.0±2.8	57.5±2.3	21.8±2.8	19.3±3.3	25.3±2.7	22.5±2.2

Impact of Learning Rate Selection Figure 2 examines the sensitivity of Fed-ADE to the choice of learning rate bounds under label shift scenarios on CIFAR-10 and Tiny ImageNet. We vary η_{\min} while fixing $\eta_{\max} = 10^{-4}$, and vary η_{\max} while fixing $\eta_{\min} = 5 \times 10^{-6}$. Across both datasets, Fed-ADE consistently maintains high accuracy within a broad range of hyperparameter choices. While extreme values lead to slight performance degradation, the overall trend shows that our dynamics-driven adaptation is far less sensitive to the exact learning rate bounds compared to fixed-rate baselines. This robustness highlights that Fed-ADE reduces the need for extensive hyperparameter tuning, an essential property in federated and online learning where search budgets are limited.

Impact of Distribution of Pre-training Data In practical federated deployments, the exact distribution of the pre-training data on the server is often unknown to clients. To examine the robustness of Fed-ADE under such realistic conditions, we evaluate post-adaptation performance on CIFAR-10 when the pre-training data follows two non-uniform distributions: *Gaussian* and *Exponential Decay*. As shown in Table 2, Fed-ADE maintains consistently strong performance across all distribution settings and shift types, with only a minor variation compared to the uniform case (cf. Table 1). These results demonstrate that our dynamics-based adaptation effectively generalizes even when the pre-training distribution differs from the assumed prior, validating its robustness under practical deployment scenarios.

Ablation Study on the Similarity Measure in Fed-ADE

Table 3 compares cosine similarity with KL divergence [1, 24, 54], Wasserstein distance [37, 57, 67], and Bayesian Check Point Detection (CPD) [14, 17, 66] under four dynamic label-shift schedules on CIFAR-10. As shown in Table 3, our cosine similarity-based Fed-ADE achieves the highest accuracy in all cases. The key reason is that cosine similarity provides a bounded and direction-based measure of drift, making it robust to noisy pseudo-labels and class imbalance that frequently arise under online shifts. In contrast, KL and Wasserstein depend on absolute probability differences and become unstable when class probabilities are near zero, while Bayesian CPD often overreacts to transient fluctuations. Thus, cosine similarity-based Fed-ADE offers the

Table 3. Ablation study on the choice of distribution-shift similarity measure in Fed-ADE under CIFAR-10 label-shift scenarios.

Measure	Lin.	Sin.	Squ.	Ber.
Fed-ADE (Cosine similarity)	73.8 ± 0.6	73.6 ± 0.5	72.2 ± 1.6	72.9 ± 2.2
KL divergence	63.2 ± 3.8	62.4 ± 2.3	61.1 ± 3.4	61.4 ± 3.6
Wasserstein	70.8 ± 0.6	69.9 ± 1.1	68.8 ± 1.3	66.5 ± 2.1
Bayesian CPD	71.5 ± 0.5	70.8 ± 0.8	69.7 ± 2.4	69.0 ± 1.1

Table 4. Ablation of Fed-ADE estimators on CIFAR-10

S_{unc}	S_{rep}	Variant	Label Shift (%)	Covariate Shift (%)
✓	✓	Fed-ADE (full)	73.8 ± 0.6	64.4 ± 0.2
✗	✓	w/o S_{unc}	71.3 ± 0.3	64.2 ± 0.1
✓	✗	w/o S_{rep}	73.1 ± 0.4	64.0 ± 0.3
✗	✗	Fixed LR	70.8 ± 2.1	63.9 ± 0.3

most stable shift signal, enabling Fed-ADE to adjust learning rates reliably across clients. The detailed description of this ablation study is provided in Appendix H.3.

Table 4 shows that both w/o S_{unc} and w/o S_{rep} underperform the full Fed-ADE across label and covariate shifts, while a fixed learning rate performs worst. This indicates that S_{unc} and S_{rep} capture complementary distribution dynamics and are both necessary for effective learning rate adaptation.

Ablation Study on Estimators in Fed-ADE

Table 4 shows that removing either estimator degrades performance under both label and covariate shifts. In particular, w/o S_{unc} leads to a noticeable drop under label shift, while w/o S_{rep} slightly reduces performance under covariate shift. The fixed learning-rate baseline performs worst and exhibits higher variance. These results indicate that S_{unc} and S_{rep} capture complementary aspects of distribution dynamics, and that combining both signals yields more stable and effective learning-rate adaptation.

7. Conclusions

We presented Fed-ADE, a novel framework for unsupervised federated post-adaptation under evolving distribution shifts. Our approach combines lightweight estimators for online distribution shifts with a theoretically grounded adaptive learning rate and a personalized federated update scheme, providing both provable dynamic regret and convergence guarantees and high practical efficiency. Beyond its methodological novelty, Fed-ADE is validated through extensive experiments on various benchmarks, covering major shift types where it consistently outperforms strong baselines. This breadth of validation highlights the robustness, versatility, and real-world readiness of our method, positioning Fed-ADE as a principled and practical foundation for advancing adaptive, shift-aware federated learning in dynamic and heterogeneous environments.

Acknowledgment

This work was supported by the National Research Foundation of Korea (NRF) grant funded by the Korean government (MSIT) under Grant RS-2025-02214082 and RS-2023-00278812.

References

- [1] Shadi Alijani and Homayoun Najjaran. WQLCP: Weighted adaptive conformal prediction for robust uncertainty quantification under distribution shifts. In *IEEE/CVF Conference on Computer Vision and Pattern Recognition*, 2025. 8
- [2] Yong Bai, YuJie Zhang, Peng Zhao, Masashi Sugiyama, and ZhiHua Zhou. Adapting to online label shift with provable guarantees. In *Advances in Neural Information Processing Systems*, 2022. 1, 2, 3, 6, 12
- [3] Sungyong Baik, Myungsub Choi, Janghoon Choi, Heewon Kim, and Kyoung Mu Lee. Meta-learning with adaptive hyperparameters. In *Advances in Neural Information Processing Systems*, 2020. 1
- [4] Wenxuan Bao, Tianxin Wei, Haohan Wang, and Jingrui He. Adaptive test-time personalization for federated learning. In *Advances in Neural Information Processing Systems*, 2023. 2
- [5] Omar Besbes, Yonatan Gur, and Assaf Zeevi. Non-stationary stochastic optimization. *Operations Research*, 63(5):1227–1244, 2015. 6
- [6] Léon Bottou, Frank Curtis, and Jorge Nocedal. Optimization methods for large-scale machine learning. *Society for Industrial and Applied Mathematics Review*, 60(2):223–311, 2018. 7
- [7] Chuang Chen, Jiantao Shi, Mouquan Shen, Ningyun Lu, Hui Yu, Yukun Chen, and Cunsong Wang. Pseudo-label guided sparse deep belief network learning method for fault diagnosis of radar critical components. *IEEE Transactions on Instrumentation and Measurement*, 72:1–12, 2023. 5
- [8] Haokun Chen, Yao Zhang, Denis Krompass, Jindong Gu, and Volker Tresp. FedDAT: An approach for foundation model finetuning in multi-modal heterogeneous federated learning. In *AAAI Conference on Artificial Intelligence*, 2024. 1
- [9] Junbao Chen, Jingfeng Xue, Yong Wang, Zhenyan Liu, and Lu Huang. Classifier clustering and feature alignment for federated learning under distributed concept drift. In *Advances in Neural Information Processing Systems*, 2024. 6, 13
- [10] Lingjiao Chen, Matei Zaharia, and James Y Zou. Estimating and explaining model performance when both covariates and labels shift. In *Advances in Neural Information Processing Systems*, 2022. 11
- [11] Il Yong Chun, Zhengyu Huang, Hongki Lim, and Jeffrey A. Fessler. Momentum-Net: Fast and convergent iterative neural network for inverse problems. *IEEE Transactions on Pattern Analysis and Machine Intelligence*, 45(4):4915–4931, 2023. 1
- [12] Liam Collins, Hamed Hassani, Aryan Mokhtari, and Sanjay Shakkottai. Exploiting shared representations for personalized federated learning. In *International Conference on Machine Learning*, 2021. 1, 2, 3
- [13] Yucong Dai, Shilin Gu, Ruidong Fan, Chao Xu, and Chenping Hou. Label shift meets online learning: Ensuring consistent adaptation with universal dynamic regret. In *IEEE/CVF Conference on Computer Vision and Pattern Recognition*, 2025. 2
- [14] Ritwik Dash and Mamata Jenamani. Outlier resilient online multivariate change point detection using subsequence divergence estimation in sensor data streams. *IEEE Sensors Journal*, 2024. 8
- [15] Chanin Eom and Minhae Kwon. Price of the autonomous strategy with reinforcement learning in mixed-autonomy traffic networks. *IEEE Transactions on Intelligent Transportation Systems*, 27(2):2741–2752, 2026. 2
- [16] Chanin Eom, Dongsu Lee, and Minhae Kwon. Selective imitation for efficient online reinforcement learning with pre-collected data. *ICT Express*, 10(6):1308–1314, 2024. 1
- [17] Mohammad Farshad. Power frequency estimation based on a bayesian online changepoint detector. *IEEE Transactions on Power Delivery*, 39(4):2541–2551, 2024. 8
- [18] Yaroslav Ganin and Victor Lempitsky. Unsupervised domain adaptation by backpropagation. In *International Conference on Machine Learning*, 2015. 2, 6, 13
- [19] Dan Hendrycks and Thomas Dietterich. Benchmarking neural network robustness to common corruptions and perturbations. In *International Conference on Learning Representations*, 2019. 6, 11, 12
- [20] Kun Jin, Tongxin Yin, Zhongzhu Chen, Zeyu Sun, Xueru Zhang, Yang Liu, and Mingyan Liu. Performative federated learning: A solution to model-dependent and heterogeneous distribution shifts. In *AAAI Conference on Artificial Intelligence*, 2024. 1
- [21] Suyeon Jin, Chaeyeon Cha, and Hyunggon Park. Alternating offer-based payment allocation for privacy non-disclosure in federated learning. *IEEE Signal Processing Letters*, 32:1500–1504, 2025. 1
- [22] Mugon Joe, Miru Kim, and Minhae Kwon. Contrastive learning based network attack classifier for imbalanced data. *Journal of Communications and Networks*, 28(1):86 – 97, 2026. 1
- [23] Sai Praneeth Karimireddy, Satyen Kale, Mehryar Mohri, Sashank Reddi, Sebastian Stich, and Ananda Theertha Suresh. SCAFFOLD: Stochastic controlled averaging for federated learning. In *International Conference on Machine Learning*, 2020. 2
- [24] Behraj Khan, Rizwan Qureshi, Nouman Muhammad Durani, and Tahir Qasim Syed. Confidence-calibrated covariate shift correction for few-shot classification in vision-language models. In *IEEE/CVF Conference on Computer Vision and Pattern Recognition*, 2025. 8
- [25] Chae Won Kim, Heewon Park, Dohyeon Kim, Yuchang Seong, Minhae Kwon, and Junil Kim. Cluvar: clustering of variants using autoencoder for inferring cancer subclones from single cell rna sequencing data. *Briefings in Bioinformatics*, 26(6):bbaf603, 2025. 1
- [26] Miru Kim, Mugon Joe, and Minhae Kwon. OASIS: Openworld adaptive self-supervised and imbalanced-aware system. In *ACM International Conference on Information and Knowledge Management*, 2025. 2

- [27] Miru Kim, Heewon Park, and Minhae Kwon. Personalized split federated learning with early-exit: Pre-training and on-line learning against label shifts. *IEEE Internet of Things Journal*, 2025. 1, 2, 3
- [28] Jueun Ko, Hyewon Park, Hyesong Choi, and Dongbo Min. RobIA: Robust instance-aware continual test-time adaptation for deep stereo. In *Advances in Neural Information Processing Systems*, 2025. 1
- [29] Alex Krizhevsky and Geoffrey Hinton. Learning multiple layers of features from tiny images. *Technical report, Univ. of Toronto*, 2009. 6, 11, 12
- [30] Jungmin Kwon and Hyunggon Park. Efficient and resilient packet recovery for federated learning via approximation. *IEEE Transactions on Mobile Computing*, 25(5), 2026. 1
- [31] Hyoseon Kye and Minhae Kwon. Partial federated learning based network intrusion system for mobile devices. In *International Symposium on Theory, Algorithmic Foundations, and Protocol Design for Mobile Networks and Mobile Computing*, pages 283–284, 2022. 1
- [32] Yann Le and Xuan Yang. Tiny imagenet visual recognition challenge. *CS 231N*, 7(7):3, 2015. 6, 11
- [33] Dongsu Lee and Minhae Kwon. Scenario-free autonomous driving with multi-task offline-to-online reinforcement learning. *IEEE Transactions on Intelligent Transportation Systems*, 26(9):13317–13330, 2025. 1
- [34] Qinbin Li, Bingsheng He, and Dawn Song. Model-contrastive federated learning. In *IEEE Conference on Computer Vision and Pattern Recognition*, 2021. 2
- [35] Tian Li, Anit Kumar Sahu, Manzil Zaheer, Maziar Sanjabi, Ameet Talwalkar, and Virginia Smith. Federated optimization in heterogeneous networks. In *Conference on Machine Learning and Systems*, 2020. 1, 2
- [36] Tian Li, Shengyuan Hu, Ahmad Beirami, and Virginia Smith. Ditto: Fair and robust federated learning through personalization. In *International Conference on Machine Learning*, 2021. 1
- [37] Wenqian Li, Shuran Fu, Fengrui Zhang, and Yan Pang. Data valuation and detections in federated learning. In *IEEE/CVF Conference on Computer Vision and Pattern Recognition*, 2024. 8
- [38] Haoyuan Liang, Xinyu Zhang, Shilei Cao, Guowen Li, and Juepeng Zheng. TTA-FedDG: Leveraging test-time adaptation to address federated domain generalization. In *Proceedings of the AAAI Conference on Artificial Intelligence*, 2025. 2
- [39] Paul Liang, Terrance Liu, Ziyin Liu, Ruslan Salakhutdinov, and Louis-Philippe Morency. Think locally, act globally: Federated learning with local and global representations. In *Advances in Neural Information Processing Systems*, 2020. 3
- [40] Zachary Lipton, Yu-Xiang Wang, and Alexander Smola. Detecting and correcting for label shift with black box predictors. In *International Conference on Machine Learning*, 2018. 3, 2
- [41] Yuxiang Lu, Suizhi Huang, Yuwen Yang, Shalayiding Sirejiding, Yue Ding, and Hongtao Lu. Fedhca2: Towards hetero-client federated multi-task learning. In *IEEE/CVF Conference on Computer Vision and Pattern Recognition*, 2024. 1
- [42] Liangchen Luo, Yuanhao Xiong, Yan Liu, and Xu Sun. Adaptive gradient methods with dynamic bound of learning rate. In *International Conference on Learning Representations*, 2019. 1
- [43] Pouya M Ghari and Yanning Shen. Personalized federated learning with mixture of models for adaptive prediction and model fine-tuning. In *Advances in Neural Information Processing Systems*, 2024. 1, 2, 6, 13
- [44] Brendan McMahan, Eider Moore, Daniel Ramage, Seth Hampson, and Blaise Aguera y Arcas. Communication-efficient learning of deep networks from decentralized data. In *International Conference on Artificial Intelligence and Statistics*, 2017. 1, 2
- [45] Sina Mohseni, Haotao Wang, Chaowei Xiao, Zhiding Yu, Zhangyang Wang, and Jay Yadawa. Taxonomy of machine learning safety: A survey and primer. *ACM Computing Surveys*, 55(8):1–38, 2022. 11
- [46] Heewon Park, Mugon Joe, Miru Kim, and Minhae Kwon. ASAP: Unsupervised post-training with label distribution shift adaptive learning rate. In *ACM International Conference on Information and Knowledge Management*, 2025. 1
- [47] Heewon Park, Miru Kim, and Minhae Kwon. Personalized federated sensing for heterogeneous environment. *IEEE Sensors Letters*, 9(4), 2026. 1, 3
- [48] Sunghyun Park, Seunghan Yang, Jaegul Choo, and Sungrack Yun. Label shift adapter for test-time adaptation under covariate and label shifts. In *IEEE/CVF International Conference on Computer Vision*, 2023. 5
- [49] Unki Park, Seongmoon Jeong, Youngchan Jang, Gyeong-Moon Park, and Jong Hwan Ko. Test-time fine-tuning of image compression models for multi-task adaptability. In *Proceedings of the Computer Vision and Pattern Recognition Conference*, 2025. 1
- [50] Fabio Petroni, Tim Rocktäschel, Patrick Lewis, Anton Bakhtin, Yuxiang Wu, Alexander H Miller, and Sebastian Riedel. Language models as knowledge bases? *arXiv preprint arXiv:1909.01066*, 2019. 6, 11
- [51] Krishna Pillutla, Kshitiz Malik, Abdel Mohamed, Mike Rabbit, Maziar Sanjabi, and Lin Xiao. Federated learning with partial model personalization. In *International Conference on Machine Learning*, 2022. 1, 2, 3, 7, 8
- [52] YuYang Qian, Yong Bai, ZhenYu Zhang, Peng Zhao, and ZhiHua Zhou. Handling new class in online label shift. In *IEEE International Conference on Data Mining*, 2023. 5
- [53] Vaibhav Rathore, Saikat Dutta, Sarthak Mehrotra, Zsolt Kira, Biplab Banerjee, et al. When domain generalization meets generalized category discovery: An adaptive task-arithmetic driven approach. In *IEEE/CVF Conference on Computer Vision and Pattern Recognition*, 2025. 2
- [54] Lijun Sheng, Jian Liang, Zilei Wang, and Ran He. R-TPT: Improving adversarial robustness of vision-language models through test-time prompt tuning. In *IEEE/CVF Conference on Computer Vision and Pattern Recognition*, 2025. 8
- [55] Haopeng Sun, Yingwei Zhang, Lumin Xu, Sheng Jin, Ping Luo, Chen Qian, Wentao Liu, and Yiqiang Chen. Unsupervised continual domain shift learning with multi-prototype modeling. In *IEEE/CVF Conference on Computer Vision and Pattern Recognition*, 2025. 2

- [56] Yiyu Sun, Chuan Guo, and Yixuan Li. ReAct: Out-of-distribution detection with rectified activations. In *Advances in Neural Information Processing Systems*, 2021. 11
- [57] Tung-Long Vuong, Hoang Phan, Vy Vo, Anh Bui, Thanh-Toan Do, Trung Le, and Dinh Phung. Preserving clusters in prompt learning for unsupervised domain adaptation. In *IEEE/CVF Conference on Computer Vision and Pattern Recognition*, 2025. 8
- [58] Ruihan Wu, Chuan Guo, Yi Su, and Kilian Weinberger. Online adaptation to label distribution shift. In *Advances in Neural Information Processing Systems*, 2021. 2, 3, 6, 12
- [59] Li Yang, Adnan Siraj Rakin, and Deliang Fan. Rep-net: Efficient on-device learning via feature reprogramming. In *IEEE/CVF Conference on Computer Vision and Pattern Recognition*, 2022. 1
- [60] Li Yang, Zhipeng Luo, Shiming Zhang, Fei Teng, and Tianrui Li. Continual learning for smart city: A survey. *IEEE Transactions on Knowledge and Data Engineering*, 2024. 1
- [61] Xiyuan Yang, Wenke Huang, and Mang Ye. FedAS: Bridging inconsistency in personalized federated learning. In *IEEE/CVF Conference on Computer Vision and Pattern Recognition*, 2024. 1, 2, 3
- [62] Changkun Ye, Russell Tsuchida, Lars Petersson, and Nick Barnes. Label Shift Estimation for Class-Imbalance Problem: A Bayesian Approach. In *IEEE/CVF International Conference on Computer Vision*, 2024. 3
- [63] Kaichao You, Mingsheng Long, Zhangjie Cao, Jianmin Wang, and Michael I Jordan. Universal domain adaptation. In *IEEE/CVF Conference on Computer Vision and Pattern Recognition*, 2019. 2, 6, 13
- [64] Zequn Zeng, Yudi Su, Jianqiao Sun, Tiansheng Wen, Hao Zhang, Zhengjue Wang, Bo Chen, Hongwei Liu, and Jiawei Ma. Explaining domain shifts in language: Concept erasing for interpretable image classification. In *IEEE/CVF Conference on Computer Vision and Pattern Recognition*, 2025. 2
- [65] Yu-Jie Zhang, Zhen-Yu Zhang, Peng Zhao, and Masashi Sugiyama. Adapting to continuous covariate shift via online density ratio estimation. In *Advances in Neural Information Processing Systems*, 2023. 11
- [66] Zeyue Zhang, Xiaoling Lu, and Feng Zhou. Conjugate bayesian two-step change point detection for hawkes process. In *Advances in Neural Information Processing Systems*, 2024. 8
- [67] Jichun Zhao, Haiyong Jiang, Haoxuan Song, Jun Xiao, and Dong Gong. D³CTTA: Domain-dependent decorrelation for continual test-time adaption of 3D LiDAR segmentation. In *IEEE/CVF Conference on Computer Vision and Pattern Recognition*, 2025. 8
- [68] Chunting Zhou, Xuezhe Ma, Paul Michel, and Graham Neubig. Examining and combating spurious features under distribution shift. In *International Conference on Machine Learning*, 2021. 1
- [69] Zhi Zhou, Lan-Zhe Guo, Lin-Han Jia, Dingchu Zhang, and Yu-Feng Li. ODS: Test-time adaptation in the presence of open-world data shift. In *International Conference on Machine Learning*, 2023. 11

Appendix - Fed-ADE: Adaptive Learning Rate for Federated Post-adaptation under Distribution Shift

Contents

6	A Notation Table	2
7	B Proof of Unbiased Risk Estimation	2
8	C Proof of Theorem 1	3
9	D Proof of Theorem 2	4
10	E Proof of Theorem 3	5
11	E.1. Regret Bound	5
12	E.2. Min-max Optimality	6
13	F. Convergence Analyses	7
14	G Simulation Settings	11
15	G.1. Datasets	11
16	G.2. Online Distribution Shift Modeling	11
17	G.3. Distribution Shift Scenarios	11
18	G.4. Compared Methods	12
19	G.5. Hyperparameters	13
20	G.6. Hardware Specifications	13
21	H Extra Simulation Results	14
22	H.1. Impact of Learning Rate Selection	14
23	H.2. Impact of Distribution of Pre-training Data	15
24	H.3. Why Cosine Similarity? Alternatives and Ablations	15

25 **A. Notation Table**

Table 5. Notation Table

Notation	Description	Notation	Description
\mathbf{x}_G^0	Pre-training data at server	\mathbf{y}_G^0	Pre-training labels at server
$\mathbf{Q}_{G,\mathbf{x}}^0$	Feature distribution of \mathbf{x}_G^0	$\mathbf{Q}_{G,\mathbf{y}}^0$	Label distribution of \mathbf{y}_G^0
\mathcal{I}	Set of class indices	i	Index for class
t	Timestep	T	Total number of timesteps
\mathcal{C}	Set of FL clients	c	Client index
θ	Global model parameters	θ_c	Model parameters of client c
\mathbf{Q}_c^t	Overall data distribution at time t	$\omega(t)$	Weighting function controlling the distribution at time t
$\mathcal{H}(\cdot)$	Softmax prediction of the model	$\mathcal{L}(\cdot)$	Loss function
$\mathcal{F}_c^{t,i}(\theta_c)$	Class-wise risk for class i	$\widehat{\mathcal{F}}_c^{0,i}(\theta_c)$	Empirical risk
\mathbf{M}	Confusion matrix computed using pre-training data	$\mathbf{Q}_{c,\widehat{\mathbf{y}}}^t$	Predicted distribution over \mathbf{x}_c^t
R	Total number of communication rounds	r	Communication round
$\mathcal{C}^{(r)}$	Selected client set in round r	N_c^t	Number of samples of client c at t
ψ_c	Shared layers of client c	ϕ_c	Personalized layers of client c
$\widehat{\psi}$	Aggregated global shared layers	$\{\psi_c, \phi_c\}$	Model split: shared/personalized
$[\eta_{\min}, \eta_{\max}]$	Min/max learning rate bounds	S^t	Distribution dynamics signal
$S_{\text{unc},c}^t$	Uncertainty dynamic signal	$S_{\text{rep},c}^t$	Representation dynamic signal
\mathbf{q}_c^t	Aggregated predictive distribution of current data batch	\mathbf{z}_c^t	Batch-level latent feature vector
$h_{\psi_c}(\cdot)$	Feature extractor	$K_{\cos}, K_h, K_\psi, K_\phi$	Lipschitz constant
B	Loss value upper bound	σ	Min. singular value of \mathbf{M}
Γ	Projection constant	$ \mathcal{I} $	Number of classes
Reg_T	Dynamic regret over T rounds	$\Delta\mathcal{L}^{(0)}$	Initial loss gap for convergence

26 **B. Proof of Unbiased Risk Estimation**

27 **Lemma 5** (Unbiased Risk Estimator). *Given model parameters θ_c independent of the test-time data $(\mathbf{x}_c^t, \mathbf{y}_c^t)$, the estimator*
 28 $\widehat{\mathcal{F}}_c^t$ *in (4) satisfies*

$$\mathbb{E}_{\mathbf{y}_c^t \sim \mathbf{Q}_{c,\mathbf{y}}^t}[\widehat{\mathcal{F}}_c^t(\theta_c)] = \mathcal{F}_c^t(\theta_c),$$

29 *provided that the confusion matrix \mathbf{M} , estimated at the server using sufficient pre-training data $(\mathbf{x}_G^0, \mathbf{y}_G^0)$ ensuring $\widehat{\mathbf{M}} = \mathbf{M}$,*
 30 *and that each client has sufficient local initial data $(\mathbf{x}_c^0, \mathbf{y}_c^0)$ such that $\widehat{\mathcal{F}}_c^0(\theta_c) = \mathcal{F}_c^0(\theta_c)$ for all $i \in \mathcal{I}$.*

31 *Proof.* The expected risk decomposes into class-specific components:

$$\mathcal{F}_c^t(\theta_c) = \sum_{i \in \mathcal{I}} [\mathbf{Q}_{\mathbf{y}_c^t}]_i \cdot \mathcal{F}_c^{0,i}(\theta_c)$$

32 where \mathcal{I} denotes the class index set. Through BBSE [40], we approximate $\mathbf{Q}_{\mathbf{y}_c^t} \approx \mathbf{M}^{-1} \mathbf{Q}_{\widehat{\mathbf{y}}_c^t}$ using the confusion matrix \mathbf{M}
 33 from pre-training and empirical predictions $\mathbf{Q}_{\widehat{\mathbf{y}}_c^t}$.

34 Expanding the estimator's expectation:

$$\mathbb{E}[\widehat{\mathcal{F}}_c^t] = \sum_{i \in \mathcal{I}} [\widehat{\mathbf{M}}^{-1} \mathbb{E}[\mathbf{Q}_{\widehat{\mathbf{y}}_c^t}]]_i \cdot \widehat{\mathcal{F}}_c^{0,i}(\theta_c)$$

35 Under condition $\mathbb{E}[\mathbf{Q}_{\widehat{\mathbf{y}}_c^t}] = \mathbf{M} \mathbf{Q}_{\mathbf{y}_c^t}$, yielding:

$$\mathbb{E}[\widehat{\mathcal{F}}_c^t] = \sum_{i \in \mathcal{I}} [\mathbf{Q}_{\mathbf{y}_c^t}]_i \cdot \mathcal{F}_c^{0,i}(\theta_c) = \mathcal{F}_c^t(\theta_c)$$

36 The estimation error $|\mathbb{E}[\widehat{\mathcal{F}}_c^t] - \mathcal{F}_c^t|$ is bounded by $\mathcal{O}(1/\sqrt{n_0})$ via concentration inequalities, where a number of pre-training
 37 data $n_0 = |(\mathbf{x}_G^0, \mathbf{y}_G^0)|$. This becomes negligible when $n_0 \geq \Omega(|\mathcal{I}|^2/\epsilon^2)$ for error tolerance ϵ . Practical implementations may
 38 employ singular value thresholding for numerical stability when inverting \mathbf{M} . \square

39 Complete derivation expanding the expectation operator:

$$\mathbb{E}_{\mathbf{x}_c^t}[\widehat{\mathcal{F}}_c^t] = \sum_{i \in \mathcal{I}} \mathbf{M}^{-1} \mathbb{E}[\mathbf{Q}_{\widehat{\mathbf{y}}_c^t}] \cdot \mathcal{F}_c^{0,i}(\theta_c) = \sum_{i \in \mathcal{I}} [\mathbf{Q}_{\mathbf{y}_c^t}]_i \cdot \mathcal{F}_c^{0,i}(\theta_c)$$

40 confirming the unbiasedness through the relationship $\mathbf{Q}_{\mathbf{y}_c^t} = \mathbf{M}^{-1} \mathbb{E}[\mathbf{Q}_{\widehat{\mathbf{y}}_c^t}]$ established via BBSE methodology.

41 **Remark 6.** The complexity function $\Omega(\cdot)$ in the sample complexity $n_0 \geq \Omega(|\mathcal{Z}|^2/\epsilon^2)$ denotes an asymptotic lower bound,
 42 meaning the pre-training dataset size must grow at least quadratically with the number of classes to guarantee estimation
 43 accuracy. This aligns with information-theoretic limits for distribution estimation.

44 C. Proof of Theorem 1

45 We restate the theorem for completeness. Let $\mathbf{Q}_{c,y}^t$ denote the true predictive distribution marginal at timestep t , and \mathbf{q}_c^t the
 46 empirical mean softmax vector defined in (11). Under ϵ -calibration with respect to $\mathbf{Q}_{c,y}^t$, we have $\|\mathbf{q}_c^t - \mathbf{Q}_{c,y}^t\|_2 \leq \epsilon_t$ in
 47 expectation. The cumulative surrogate of predictive dynamics is

$$\bar{\mathcal{S}}_{\text{unc}} = \sum_{t=1}^T \mathcal{S}_{\text{unc}}^t = \sum_{t=1}^T (1 - \cos(\mathbf{q}_c^{t-1}, \mathbf{q}_c^t)).$$

48 Our goal is to show that $\bar{\mathcal{S}}_{\text{unc}}$ approximates the cumulative true deviation $\sum_{t=1}^T \|\mathbf{Q}_{c,y}^t - \mathbf{Q}_{c,y}^{t-1}\|_1$ up to an additive error of
 49 order $\mathcal{O}(\sum_t \epsilon_t)$.

50 **Step 1: Lipschitz continuity of cosine distance.** The cosine similarity function $\cos(\cdot, \cdot)$ is K_{\cos} -Lipschitz continuous in
 51 each of its arguments on the unit sphere, i.e.,

$$|\cos(\mathbf{a}, \mathbf{b}) - \cos(\mathbf{a}', \mathbf{b}')| \leq K_{\cos}(\|\mathbf{a} - \mathbf{a}'\|_2 + \|\mathbf{b} - \mathbf{b}'\|_2).$$

52 Since both \mathbf{q}_c^t and $\mathbf{Q}_{c,y}^t$ are probability vectors normalized to unit norm, this Lipschitz property holds directly.

53 **Step 2: Bounding the surrogate deviation.** By the definition of $\mathcal{S}_{\text{unc}}^t$, we have

$$\begin{aligned} & |\mathcal{S}_{\text{unc}}^t - (1 - \cos(\mathbf{Q}_{c,y}^{t-1}, \mathbf{Q}_{c,y}^t))| \\ & \leq K_{\cos}(\|\mathbf{q}_c^{t-1} - \mathbf{Q}_{c,y}^{t-1}\|_2 + \|\mathbf{q}_c^t - \mathbf{Q}_{c,y}^t\|_2) \leq K_{\cos}(\epsilon_{t-1} + \epsilon_t). \end{aligned}$$

54 **Step 3: Summing over timesteps.** Summing over $t = 2, \dots, T$ yields

$$\left| \sum_{t=1}^T \mathcal{S}_{\text{unc}}^t - \sum_{t=1}^T (1 - \cos(\mathbf{Q}_{c,y}^{t-1}, \mathbf{Q}_{c,y}^t)) \right| \leq K_{\cos} \sum_{t=2}^T (\epsilon_t + \epsilon_{t-1}).$$

55 **Step 4: Relating cosine distance to total variation.** For normalized probability vectors, the cosine distance upper bounds
 56 the ℓ_1 deviation:

$$1 - \cos(\mathbf{Q}_{c,y}^{t-1}, \mathbf{Q}_{c,y}^t) \leq \|\mathbf{Q}_{c,y}^{t-1} - \mathbf{Q}_{c,y}^t\|_1.$$

57 Combining this with the bound above yields

$$\left| \bar{\mathcal{S}}_{\text{unc}} - \sum_{t=1}^T \|\mathbf{Q}_{c,y}^{t-1} - \mathbf{Q}_{c,y}^t\|_1 \right| \leq K_{\cos} \sum_{t=2}^T (\epsilon_t + \epsilon_{t-1}).$$

58

□

59 **D. Proof of Theorem 2**

60 Let \mathbf{z}_c^t denote the empirical ℓ_2 -normalized batch-mean feature vector defined in (13), and $\bar{\mathbf{z}}_c^t = \mathbb{E}[h_{\psi_c}(x)/\|h_{\psi_c}(x)\|_2]$ be its
 61 expectation under the local distribution at time t . We assume $\|\mathbf{z}_c^t - \bar{\mathbf{z}}_c^t\|_2 \leq \epsilon'_t$ in expectation, and that the shared representation
 62 extractor h_{ψ_c} is K_h -Lipschitz.

63 The cumulative surrogate of representation dynamics is defined as

$$\bar{\mathcal{S}}_{\text{rep}} = \sum_{t=1}^T \mathcal{S}_{\text{rep}}^t = \frac{1}{2} \sum_{t=1}^T (1 - \cos(\mathbf{z}_c^{t-1}, \mathbf{z}_c^t)).$$

64 Since all feature vectors are ℓ_2 -normalized, the cosine distance $\frac{1}{2}(1 - \cos(\mathbf{a}, \mathbf{b}))$ is smooth on the unit sphere, and its deviation
 65 with respect to small perturbations of \mathbf{a} and \mathbf{b} is bounded linearly by their ℓ_2 distance. Using the Lipschitz continuity of h_{ψ_c} ,
 66 the deviation between the empirical mean \mathbf{z}_c^t and its population counterpart $\bar{\mathbf{z}}_c^t$ thus induces a bounded perturbation in the
 67 cosine term.

68 For each timestep t , we have

$$\left| \mathcal{S}_{\text{rep}}^t - \frac{1}{2}(1 - \cos(\bar{\mathbf{z}}_c^{t-1}, \bar{\mathbf{z}}_c^t)) \right| \leq K_h(\epsilon'_{t-1} + \epsilon'_t).$$

69 Summing over all $t = 2, \dots, T$ gives

$$\left| \sum_{t=1}^T \mathcal{S}_{\text{rep}}^t - \sum_{t=1}^T \frac{1}{2}(1 - \cos(\bar{\mathbf{z}}_c^{t-1}, \bar{\mathbf{z}}_c^t)) \right| \leq K_h \sum_{t=2}^T (\epsilon'_t + \epsilon'_{t-1}).$$

70 Therefore, the cumulative surrogate $\bar{\mathcal{S}}_{\text{rep}}$ satisfies

$$\left| \bar{\mathcal{S}}_{\text{rep}} - \sum_{t=1}^T \frac{1}{2} \left(1 - \frac{\langle \bar{\mathbf{z}}_c^{t-1}, \bar{\mathbf{z}}_c^t \rangle}{\|\bar{\mathbf{z}}_c^{t-1}\|_2 \|\bar{\mathbf{z}}_c^t\|_2} \right) \right| \leq K_h \sum_{t=2}^T (\epsilon'_t + \epsilon'_{t-1}),$$

71 which shows that $\bar{\mathcal{S}}_{\text{rep}}$ accurately approximates the temporal trajectory of the expected local feature representations, with error
 72 bounded by the feature-level estimation noise scaled by the Lipschitz constant K_h . \square

73 E. Proof of Theorem 3

74 E.1. Regret Bound

75 We present the proof of Theorem 3 by decomposing the dynamic regret into two terms. Our approach introduces a reference
76 sequence that evolves in a piecewise-constant manner across predefined intervals. The first term evaluates the algorithm's
77 performance relative to this sequence, while the second term quantifies how well the reference sequence itself approximates
78 the optimal comparator. For the following proof, we use $\{\psi_c^t, \phi_c^t\}$ for model parameters to differentiate the model per timestep.

79 *Proof.* The regret bound can be split into two terms by introducing a reference sequence $\{\psi_c^t, \phi_c^t\}$ that only changes every
80 τ steps. Specifically, let $\mathcal{J}_m = [(m-1)\tau + 1, m\tau]$ denote the m -th interval. For each interval, the comparator $\{\psi_c^t, \phi_c^t\}$
81 is chosen as the best fixed decision in that interval, i.e., $\{\psi_c^{\mathcal{J}_m}, \phi_c^{\mathcal{J}_m}\} = \arg \min_{\{\psi_c^t, \phi_c^t\}} \sum_{t \in \mathcal{J}_m} \mathcal{F}_c^t(\{\psi_c^t, \phi_c^t\})$ for $t \in \mathcal{J}_m$.
82 Then,

$$\begin{aligned} & \mathbb{E}_{1:T} \left[\sum_{t=1}^T \mathcal{F}_c^t(\{\psi_c^t, \phi_c^t\}) - \sum_{t=1}^T \mathcal{F}_c^t(\{\psi_c^*, \phi_c^*\}) \right] \\ &= \mathbb{E}_{1:T} \left[\sum_{t=1}^T \mathcal{F}_c^t(\{\psi_c^t, \phi_c^t\}) - \sum_{m=1}^M \sum_{t \in \mathcal{J}_m} \mathcal{F}_c^t(\{\psi_c^{\mathcal{J}_m}, \phi_c^{\mathcal{J}_m}\}) \right] \end{aligned} \quad (a)$$

$$+ \mathbb{E}_{1:T} \left[\sum_{m=1}^M \sum_{t \in \mathcal{J}_m} \mathcal{F}_c^t(\{\psi_c^{\mathcal{J}_m}, \phi_c^{\mathcal{J}_m}\}) - \sum_{t=1}^T \mathcal{F}_c^t(\{\psi_c^*, \phi_c^*\}) \right] \quad (b)$$

83 where $M = \lceil \frac{T}{\tau} \rceil \leq T/\tau + 1$ is the number of intervals. Next, we analyze term (a) and term (b) separately.

84 **Analysis of term (a)** This term represents the regret of the algorithm compared to the piecewise-stationary reference
85 sequence. The regret with respect to the expected risk $\mathcal{F}_c^t(\cdot)$ can be related to the unbiased empirical risk estimator $\widehat{\mathcal{F}}_c^t(\cdot)$:

$$\begin{aligned} \text{term (a)} &= \mathbb{E}_{1:T} \left[\sum_{t=1}^T \mathcal{F}_c^t(\{\psi_c^t, \phi_c^t\}) - \sum_{t=1}^T \mathcal{F}_c^t(\{\psi_c^t, \phi_c^t\}) \right] \\ &\leq \mathbb{E}_{1:T} \left[\sum_{t=1}^T \langle \nabla \mathcal{F}_c^t(\{\psi_c^t, \phi_c^t\}), (\{\psi_c^t, \phi_c^t\}) - (\{\psi_c^t, \phi_c^t\}) \rangle \right] \\ &= \mathbb{E}_{1:T} \left[\sum_{t=1}^T \langle \nabla \mathcal{F}_c^t(\{\psi_c^t, \phi_c^t\}) - \nabla \widehat{\mathcal{F}}_c^t(\{\psi_c^t, \phi_c^t\}), (\{\psi_c^t, \phi_c^t\}) - (\{\psi_c^t, \phi_c^t\}) \rangle \right] \\ &\quad + \mathbb{E}_{1:T} \left[\sum_{t=1}^T \langle \nabla \widehat{\mathcal{F}}_c^t(\{\psi_c^t, \phi_c^t\}), (\{\psi_c^t, \phi_c^t\}) - (\{\psi_c^t, \phi_c^t\}) \rangle \right], \end{aligned}$$

86 where the first inequality uses the convexity of $\mathcal{F}_c^t(\cdot)$. The first term above is zero because $\widehat{\mathcal{F}}_c^t$ is an unbiased estimator,
87 i.e., $\nabla \mathcal{F}_c^t(\{\psi_c^t, \phi_c^t\}) = \mathbb{E}_t[\nabla \widehat{\mathcal{F}}_c^t(\{\psi_c^t, \phi_c^t\}) \mid 1 : t-1]$. For the model sequence $\{\{\psi_c^t, \phi_c^t\}\}_{t=1}^T$ generated by Fed-ADE, the
88 following lemma holds:

89 **Lemma 7.** *Under the assumptions of Theorem 3, Fed-ADE with learning rate $\eta > 0$ in equation (6) satisfies*

$$\sum_{t=1}^T \left\langle \nabla \widehat{\mathcal{F}}_c^t(\{\psi_c^t, \phi_c^t\}), (\{\psi_c^t, \phi_c^t\}) - (\{\psi_c^t, \phi_c^t\}) \right\rangle \leq \frac{2\eta|\mathcal{I}|G^2T}{\sigma^2} + \frac{2\Gamma P_T + \Gamma^2}{2\eta},$$

90 where $P_T = \sum_{t=2}^T \|(\{\psi_c^t, \phi_c^t\}) - (\{\psi_c^{t-1}, \phi_c^{t-1}\})\|_2$ is the total variation of the comparator sequence and $G \triangleq$
91 $\sup_{(\mathbf{x}_c^t, \mathbf{y}_c^t)} \|\nabla_{\{\psi_c, \phi_c\}} \mathcal{L}(\mathcal{H}(\{\psi_c, \phi_c\}, \mathbf{x}_c^t), \mathbf{y}_c^t)\|_2$ is an upper bound on the gradient norm.

92 Since the comparator sequence for term (a) changes only $M-1$ times, $P_T \leq \Gamma(M-1) \leq (\Gamma T)/\tau$. Taking expectations
93 gives

$$\text{term (a)} \leq \frac{2\eta|\mathcal{I}|G^2T}{\sigma^2} + \frac{2\Gamma^2T/\tau + \Gamma^2}{2\eta}.$$

94 **Analysis of term (b)** This term accounts for the error from changing the reference sequence. Following [5], we get

$$\text{term (b)} \leq 2\tau \sum_{t=2}^T \sup_{\{\psi_c^t, \phi_c^t\}} |\mathcal{F}_c^t(\{\psi_c^t, \phi_c^t\}) - \mathcal{F}_c^{t-1}(\{\psi_c^t, \phi_c^t\})| \triangleq 2\tau \bar{\mathcal{S}}_c.$$

95 Combining the two terms, we obtain

$$\begin{aligned} \mathbb{E}_{1:T} \left[\sum_{t=1}^T \mathcal{F}_c^t(\{\psi_c^t, \phi_c^t\}) \right] - \sum_{t=1}^T \mathcal{F}_c^t(\{\psi_c^*, \phi_c^*\}) &\leq \frac{2\eta|\mathcal{I}|G^2T}{\sigma^2} + \frac{2\Gamma^2T/\tau + \Gamma^2}{2\eta} + 2B\tau\bar{\mathcal{S}}_c \\ &\leq \left(\frac{2|\mathcal{I}|G^2}{\sigma^2} + 2B^2 \right) \eta T + \frac{\Gamma^2}{\eta} + 4(\Gamma + 1) \sqrt{\frac{BT\bar{\mathcal{S}}_c}{\eta}}, \end{aligned}$$

96 where we set $\tau = \left\lceil \sqrt{\Gamma^2T/(\eta B\bar{\mathcal{S}}_c)} \right\rceil$ for optimal balance and $B \triangleq \sup_{(\mathbf{x}_c^t, \mathbf{y}_c^t)} |\mathcal{L}(\mathcal{H}(\{\psi_c, \phi_c\}, \mathbf{x}_c^t), \mathbf{y}_c^t)|$ is an upper bound
97 on the loss value, and G represents gradient norm upper bound.

98 Under the distribution shift assumption, the variation $\bar{\mathcal{S}}_c$ can be further bounded by the change in class and representation
99 priors. Thus,

$$\mathbb{E}[\text{Reg}_T] \leq \left(\frac{2|\mathcal{I}|G^2}{\sigma^2} + 2B^2 \right) \eta T + \frac{\Gamma^2}{\eta} + 4(\Gamma + 1) \sqrt{\frac{BT\bar{\mathcal{S}}_c}{\eta}}.$$

100

□

101 E.2. Min-max Optimality

102 For online convex optimization with general convex losses, [5] showed that the dynamic regret has a lower bound of
103 $\Omega(\bar{\mathcal{S}}_c^{1/3}T^{2/3})$ when only noisy feedback is observed. Here, $\bar{\mathcal{S}}_c$ measures the total variation of the loss functions. The upper
104 bound in Theorem 3 matches this rate, showing that Fed-ADE achieves min-max optimality up to constants.

105 **Lemma 8.** *Under the same assumptions as Theorem 3, Fed-ADE with learning rate η satisfies*

$$\mathbb{E}[\text{Reg}_T] \leq 2 \left(\frac{|\mathcal{I}|G^2}{\sigma^2} + B^2 \right) \eta T + \frac{\Gamma^2}{\eta} + 4(\Gamma + 1) \sqrt{\frac{B\bar{\mathcal{S}}_cT}{\eta}} = \mathcal{O} \left(\eta T + \frac{1}{\eta} + \frac{\sqrt{\bar{\mathcal{S}}_cT}}{\eta} \right),$$

106 where $\sigma > 0$ is the minimum singular value of the confusion matrix \mathbf{M} and $\bar{\mathcal{S}}_c$ is the temporal variation of the loss.

107 This result follows by setting $\eta = \Theta(T^{-1/3}\bar{\mathcal{S}}_c^{1/3})$, which yields $\mathcal{O}(\bar{\mathcal{S}}_c^{1/3}T^{2/3})$ regret, matching the lower bound. Similar
108 reasoning shows that the algorithm also achieves $\mathcal{O}(\max\{\bar{\mathcal{S}}_c^{1/3}T^{2/3}, \sqrt{T}\})$ dynamic regret.

109 F. Convergence Analyses

110 We next show that our Fed-ADE provably converges when each per-timestep learning rate $\eta_c^t \in [\eta_{min}, \eta_{max}]$ obeys the same
111 upper bound used in Theorem 12. For the proof, we use three commonly used assumptions [6, 51] as follows.

112 **Assumption 9.** (Lipschitz parameter) For every client c , the loss function \mathcal{L} is continuously differentiable and there exist
113 Lipschitz constants $K_\psi, K_\phi, K_{\psi\phi}, K_{\phi\psi}$ holds that

- 114 • $\nabla_\psi \mathcal{L}(\bar{\psi}^{(r)}, \phi_c^{(r)})$ is K_ψ Lipschitz with respect to ψ and $K_{\psi\phi}$ Lipschitz with respect to $\phi_c^{(r)}$.
- 115 • $\nabla_\phi \mathcal{L}(\bar{\psi}^{(r)}, \phi_c^{(r)})$ is K_ϕ Lipschitz with respect to ϕ and $K_{\phi\psi}$ Lipschitz with respect to $\bar{\psi}^{(r)}$.

116 When the average loss function of total clients is defined as $\mathcal{L}(\bar{\psi}^{(r)}, \phi^{(r)}) = \frac{1}{|\mathcal{C}|} \sum_{c \in \mathcal{C}} \mathbb{E}[\mathcal{L}(\bar{\psi}^{(r)}, \phi_c^{(r)})]$, it has Lipschitz
117 constant K_ψ with respect to $\bar{\psi}^{(r)}$, $K_{\phi\psi}/\sqrt{|\mathcal{C}|}$ with respect to $\phi^{(r)}$, and $K_{\psi\phi}/|\mathcal{C}|$ with respect to any $\phi_c^{(r)}$. Further, there exist
118 χ to measure the relative cross-sensibility of $\nabla_\phi \mathcal{L}(\bar{\psi}^{(r)}, \phi_c^{(r)})$ and $\nabla_\psi \mathcal{L}(\bar{\psi}^{(r)}, \phi_c^{(r)})$ as follows.

$$\chi = \frac{\max\{K_{\psi\phi}, K_{\phi\psi}\}}{\sqrt{K_\psi K_\phi}} \quad (19)$$

120 **Assumption 10.** (Bounded variance) The stochastic gradients in the client-side update algorithm are unbiased and have
121 bounded variance as follows.

$$\mathbb{E}[\tilde{\nabla}_\phi \mathcal{L}(\bar{\psi}^{(r)}, \phi_c^{(r)})] = \nabla_\phi \mathcal{L}(\bar{\psi}^{(r)}, \phi_c^{(r)}) \quad (20)$$

$$\mathbb{E}[\tilde{\nabla}_\psi \mathcal{L}(\bar{\psi}^{(r)}, \phi_c^{(r)})] = \nabla_\psi \mathcal{L}(\bar{\psi}^{(r)}, \phi_c^{(r)}) \quad (21)$$

123 Furthermore, there exist constants σ_ϕ and σ_ψ that meet the following inequation.

$$\mathbb{E}[\|\tilde{\nabla}_\phi \mathcal{L}(\bar{\psi}^{(r)}, \phi_c^{(r)}) - \nabla_\phi \mathcal{L}(\bar{\psi}^{(r)}, \phi_c^{(r)})\|^2] \leq \sigma_\phi^2 \quad (22)$$

$$\mathbb{E}[\|\tilde{\nabla}_\psi \mathcal{L}(\bar{\psi}^{(r)}, \phi_c^{(r)}) - \nabla_\psi \mathcal{L}(\bar{\psi}^{(r)}, \phi_c^{(r)})\|^2] \leq \sigma_\psi^2 \quad (23)$$

125 We can consider $\nabla_\psi \mathcal{L}_c(\bar{\psi}^{(r)}, \phi_c^{(r)})$ as a stochastic partial gradient of average loss function $\mathcal{L}(\bar{\psi}^{(r)}, \phi^{(r)})$ with respect to $\bar{\psi}^{(r)}$.

126 **Assumption 11.** (Partial gradient diversity) There exist constants $\delta \geq 0$ and $\rho \geq 0$ such that for $\bar{\psi}^{(r)}$ and all personalized
127 layers $\phi^{(r)} = [\phi_1^{(r)}, \phi_2^{(r)}, \dots]$, which meet the following equations.

$$\frac{1}{|\mathcal{C}|} \sum_{c \in \mathcal{C}} \|\nabla_\psi \mathcal{L}(\bar{\psi}^{(r)}, \phi_c^{(r)}) - \nabla_\psi \mathcal{L}(\bar{\psi}^{(r)}, \phi^{(r)})\|^2 \leq \delta^2 + \rho^2 \|\nabla_\psi \mathcal{L}(\bar{\psi}^{(r)}, \phi^{(r)})\|^2 \quad (24)$$

128 Additionally, $\mathcal{L}(\bar{\psi}, \phi^{(r)})$ is bounded below by $\hat{\mathcal{L}}$, where $\hat{\mathcal{L}}$ meets the equation $\Delta \mathcal{L}^{(0)} = \mathcal{L}(\bar{\psi}^{(0)}, \phi^{(0)}) - \hat{\mathcal{L}}$ at initial communi-
129 cation round.

130 **Theorem 12.** The convergence of the Fed-ADE is bounded as follows, where $\Delta \mathcal{L}^{(0)}$ denotes the difference between a bound
131 and initial value of loss $\mathcal{L}(\bar{\psi}, \phi_c)$.²

$$\frac{1}{R} \sum_{r=0}^{R-1} \left(\frac{1}{K_\psi} \mathbb{E}[\Delta_\psi^{(r)}] + \frac{|\mathcal{C}^{(r)}|}{|\mathcal{C}| K_\phi} \mathbb{E}[\Delta_\phi^{(r)}] \right) \leq \frac{\Delta \mathcal{L}^{(0)}}{\eta R} + \eta \sigma_1^2 + \eta^2 \sigma_2^2 \quad (25)$$

132 Here, the constants σ_1^2 and σ_2^2 are defined as follows.

$$\sigma_1^2 = \frac{\delta^2}{K_\psi} \left(1 - \frac{|\mathcal{C}^{(r)}|}{|\mathcal{C}|} \right) + \frac{\sigma_\psi^2}{K_\psi} + \frac{\sigma_\phi^2 (|\mathcal{C}^{(r)}| + \chi^2 (|\mathcal{C}| - |\mathcal{C}^{(r)}|))}{K_\phi |\mathcal{C}|} \quad (26)$$

$$\sigma_2^2 = \left(\frac{\sigma_\psi^2 + \delta^2}{K_\psi} + \frac{\sigma_\phi^2 |\mathcal{C}^{(r)}|}{K_\phi |\mathcal{C}|} \right) (1 - E^{-1}) + \frac{\chi^2 \sigma_\phi^2}{K_\phi} \quad (27)$$

²To simplify the inequality in the following assumptions and theorems, we use following shorthands: $\phi^{(r)} = \{\phi_c^{(r)} | c \in \mathcal{C}^{(r)}\}$, $\mathcal{L}(\bar{\psi}^{(r)}, \phi_c^{(r)}) = \mathcal{L}(\{\bar{\psi}^{(r)}, \phi_c^{(r)}\}; \mathbf{x}_c^t)$, $\mathcal{L}(\bar{\psi}^{(r)}, \phi^{(r)}) = \sum_{c \in \mathcal{C}} \frac{N_c}{N} \mathcal{L}(\bar{\psi}^{(r)}, \phi_c^{(r)})$, $\Delta_\psi^{(r)} = \|\nabla_\psi \sum_{c \in \mathcal{C}} \frac{N_c}{N} \mathcal{L}(\bar{\psi}^{(r)}, \phi_c^{(r)})\|^2$, $\Delta_\phi^{(r)} = \frac{1}{|\mathcal{C}|} \sum_{c \in \mathcal{C}} \|\nabla_\phi \mathcal{L}(\bar{\psi}^{(r)}, \phi_c^{(r)})\|^2$.

133 This convergence is bounded when the learning rates are chosen as $\eta_\psi = \eta/(K_\psi E)$ and $\eta_\phi = \eta/(K_\phi E)$, where η satisfies
 134 the following inequality.

$$\eta \leq \min \left\{ \frac{1}{24(1+\rho^2)}, \frac{|\mathcal{C}^{(r)}|}{128\chi^2(|\mathcal{C}| - |\mathcal{C}^{(r)}|)}, \sqrt{\frac{|\mathcal{C}^{(r)}|}{\chi^2|\mathcal{C}|}} \right\} \quad (28)$$

135 *Proof.* The proof of Theorem 12 begins with the following equation describing the update from round r to round $r + 1$.

$$\mathcal{L}(\psi^{(r+1)}, \phi^{(r+1)}) - \mathcal{L}(\bar{\psi}^{(r)}, \phi^{(r)}) = \mathcal{L}(\bar{\psi}^{(r)}, \phi^{(r+1)}) - \mathcal{L}(\bar{\psi}^{(r)}, \phi^{(r)}) \quad (29)$$

$$+ \mathcal{L}(\psi^{(r+1)}, \phi^{(r+1)}) - \mathcal{L}(\bar{\psi}^{(r)}, \phi^{(r+1)}) \quad (30)$$

136 In the case of the update for the personalized layers in (29), since each client is training with their own data, it can be
 137 demonstrated similarly to the gradient update in conventional deep learning approaches. However, in the case of the update for
 138 the shared layers in (30), as gradient descent is performed for different client models, we aim to establish its convergence.

139 The smoothness bound for the updating of the shared layers gives an equation as follows.

$$\begin{aligned} \mathcal{L}(\psi^{(r+1)}, \phi^{(r+1)}) - \mathcal{L}(\bar{\psi}^{(r)}, \phi^{(r+1)}) &\leq \left\langle \nabla_\psi \mathcal{L}(\bar{\psi}^{(r)}, \phi^{(r+1)}), \psi^{(r+1)} - \bar{\psi}^{(r)} \right\rangle \\ &+ \frac{K_\psi}{2} \|\psi^{(r+1)} - \bar{\psi}^{(r)}\|^2 \end{aligned} \quad (31)$$

140 According to Lipschitz continuity, we can express the gradient as shown in the (31), when $\langle A, B \rangle$ means $A^T B$. The proof
 141 proceeds by demonstrating that for all communication rounds $0 < r < R$, the total sum of this gradient does not diverge but
 142 rather remains bounded, as is well known. However, a key distinction between the conventional deep learning approach and
 143 the personalized federated learning method is that only a subset of clients among the total clients participate in training during
 144 a single round. In these conditions, the virtual full participants $\tilde{\phi}^{(r+1)}$ are used to move all the dependencies of the model
 145 update on the participants $\mathcal{C}^{(r)} \in \mathcal{C}$ [51]. When applying the virtual full participants to the (31), we can get an equation as
 146 follows.

$$\begin{aligned} \left\langle \nabla_\psi \mathcal{L}(\bar{\psi}^{(r)}, \phi^{(r+1)}), \psi^{(r+1)} - \bar{\psi}^{(r)} \right\rangle &= \left\langle \nabla_\psi \mathcal{L}(\bar{\psi}^{(r)}, \tilde{\phi}^{(r+1)}), \psi^{(r+1)} - \psi^{(r)} \right\rangle \\ &+ \left\langle \nabla_\psi \mathcal{L}(\bar{\psi}^{(r)}, \tilde{\phi}^{(r+1)}) - \nabla_\psi \mathcal{L}(\bar{\psi}^{(r)}, \phi^{(r+1)}), \psi^{(r+1)} - \bar{\psi}^{(r)} \right\rangle \end{aligned} \quad (32)$$

147 Applying Young's inequality and Lipschitz inequality to the (32), the (31) can be expressed as follows.

$$\begin{aligned} \mathcal{L}(\psi^{(r+1)}, \phi^{(r+1)}) - \mathcal{L}(\bar{\psi}^{(r)}, \phi^{(r+1)}) &\leq \left\langle \nabla_\psi \mathcal{L}(\bar{\psi}^{(r)}, \phi^{(r+1)}), \psi^{(r+1)} - \bar{\psi}^{(r)} \right\rangle \\ &+ \frac{1}{2K_\psi} \|\nabla_\psi \mathcal{L}(\bar{\psi}^{(r)}, \tilde{\phi}^{(r+1)}) - \nabla_\psi \mathcal{L}(\bar{\psi}^{(r)}, \phi^{(r+1)})\|^2 \\ &+ K_\psi \|\psi^{(r+1)} - \bar{\psi}^{(r)}\|^2 \end{aligned} \quad (33)$$

148 This allows us to take an expectation. Therefore, the final bounded form can be described as follows with Assumption 11,
 149 where the $\tilde{\Delta}_\psi^{(r)}$ is the analog of $\Delta_\psi^{(r)}$ with the virtual variable $\tilde{\phi}^{(r+1)}$.

$$\frac{1}{R} \sum_{r=0}^{R-1} \left(\frac{\eta_\psi E}{8} \mathbb{E}[\tilde{\Delta}_\psi^{(r)}] + \frac{\eta_\phi E c}{16|\mathcal{C}|} \mathbb{E}[\Delta_\phi^{(r)}] \right) \leq \frac{\Delta \mathcal{L}^{(0)}}{R} + \mathcal{O}(\eta_\psi^2 + \eta_\phi^2). \quad (34)$$

150 **Bound of shared layers update** When using (34), the update of the shared layers can be bounded as follows.

$$\begin{aligned} &\mathcal{L}(\psi^{(r+1)}, \phi^{(r+1)}) - \mathcal{L}(\psi^{(r)}, \phi^{(r+1)}) \\ &\leq \left\langle \nabla_p \mathcal{L}(\psi^{(r)}, \tilde{\phi}^{(r+1)}), \psi^{(r+1)} - \psi^{(r)} \right\rangle K_\psi \|\psi^{(r+1)} - \psi^{(r)}\|^2 + \frac{\chi^2 K_\phi}{2|\mathcal{C}|} \sum_{c \in \mathcal{C}} \|\tilde{\phi}_c^{(r+1)} - \phi_c^{(r+1)}\|^2 \end{aligned} \quad (35)$$

151 Thus, the dependence of the second line term on $\phi^{(r+1)}$ is successfully eliminated. To bind the third line term, expectation can
 152 be used as follows.

$$\begin{aligned}
& \mathbb{E} \left[\mathcal{L}(\psi^{(r+1)}, \phi^{(r+1)}) - \mathcal{L}(\psi^{(r)}, \phi^{(r+1)}) \right] \\
& \leq -\frac{\eta_\psi E}{4} \mathbb{E}[\tilde{\Delta}_\psi^{(r)}] + \frac{2\eta_\psi K_\psi^2}{|\mathcal{C}|} \sum_{c \in \mathcal{C}} \sum_{e=0}^E \mathbb{E} \|\tilde{\psi}_{c,e}^{(r)} - \psi^{(r)}\|^2 + 4\eta_\phi^2 E^2 K_\phi \sigma_\phi^2 \chi^2 \left(1 - \frac{|\mathcal{C}^{(r)}|}{|\mathcal{C}|}\right) \\
& \quad + \frac{K_\psi \eta_\psi^2 E^2}{|\mathcal{C}^{(r)}|} \left(\sigma_\psi^2 + 3\delta^2 \left(1 - \frac{|\mathcal{C}^{(r)}|}{|\mathcal{C}|}\right)\right) + 8\eta_\psi^2 E^2 K_\phi \chi^2 \left(1 - \frac{|\mathcal{C}^{(r)}|}{|\mathcal{C}|}\right) \Delta_\phi^{(r)}
\end{aligned} \tag{36}$$

153 Note that $24K_\psi \eta_\psi E(1 + \rho^2) \leq 1$ is used to simplify the coefficients of some of the terms above. The term in the third line is
 154 referred to as client shift in the literature. This term can be described using the virtual variable $\tilde{\phi}^{(r+1)}$ as follows.

$$\begin{aligned}
& \frac{2\eta_\psi K_\psi^2}{|\mathcal{C}|} \sum_{c \in \mathcal{C}} \sum_{e=0}^E \mathbb{E} \|\tilde{\psi}_{c,e}^{(r)} - \psi^{(r)}\|^2 \\
& \leq \frac{16\eta_\psi^3 K_\psi^2 E(E-1)}{|\mathcal{C}|} \left(\delta^2 + \rho^2 \mathbb{E} \|\nabla_\psi \mathcal{L}(\psi^{(r)}, \tilde{\phi}^{(r+1)})\|^2\right) + 8\eta_\psi^3 K_\psi^2 E^2 (E-1) \sigma_\psi^2
\end{aligned} \tag{37}$$

155 By inputting (37) into the previous inequality of expectation (36), the inequality can be described as follows.

$$\begin{aligned}
& \mathbb{E}[\mathcal{L}(\psi^{(r+1)}, \phi^{(r+1)}) - \mathcal{L}(\psi^{(r)}, \phi^{(r+1)})] \\
& \leq -\frac{\eta_\psi E}{8} \mathbb{E}[\tilde{\Delta}_\psi^{(r)}] + \frac{K_\psi \eta_\psi^2 E^2}{|\mathcal{C}^{(r)}|} \left(\sigma_\psi^2 + 2\delta^2 \left(1 - \frac{|\mathcal{C}^{(r)}|}{|\mathcal{C}|}\right)\right) + 4\eta_\phi^2 E^2 K_\phi \sigma_\phi^2 \chi^2 \left(1 - \frac{|\mathcal{C}^{(r)}|}{|\mathcal{C}|}\right) \\
& \quad + 8\eta_\phi^2 E^2 K_\phi \chi^2 \left(1 - \frac{|\mathcal{C}^{(r)}|}{|\mathcal{C}|}\right) \Delta_\phi^{(r)} + 8\eta_\psi^2 K_\psi^3 E^2 \left(1 - \frac{|\mathcal{C}^{(r)}|}{|\mathcal{C}|}\right) (\sigma_\psi^2 + 2\delta_\psi)
\end{aligned} \tag{38}$$

156 **Bound of personalized layers** The above analysis for updating the shared layers can be applied to updating the personalized
 157 layers. This analysis provides the following, which displays the bound of the update of the personalized layers. It can be
 158 simplified some coefficients using $128\eta_\phi E K_\phi \chi^2 \left(\frac{|\mathcal{C}|}{|\mathcal{C}^{(r)}|} - 1\right) \leq 1$.

$$\begin{aligned}
& \mathbb{E} \left[\mathcal{L}(\phi^{(r+1)}, \psi^{(r+1)}) - \mathcal{L}(\psi^{(r)}, \phi^{(r)}) \right] \\
& \leq -\frac{\eta_\psi E}{8} \mathbb{E}[\tilde{\Delta}_\psi^{(r)}] - \frac{\eta_\phi E |\mathcal{C}^{(r)}|}{16|\mathcal{C}|} \mathbb{E}[\Delta_\phi^{(r)}] + 4\eta_\phi^2 K_\phi E^2 \sigma_\phi^2 \left(\frac{|\mathcal{C}^{(r)}|}{|\mathcal{C}|} + \chi^2 \left(1 - \frac{|\mathcal{C}^{(r)}|}{|\mathcal{C}|}\right)\right) \\
& \quad + \frac{\eta_\psi^2 K_\psi E^2}{|\mathcal{C}^{(r)}|} \left(\sigma_\psi^2 + 2\delta^2 \left(1 - \frac{|\mathcal{C}^{(r)}|}{|\mathcal{C}|}\right)\right) + 8\eta_\psi^2 K_\psi^2 E^2 (E-1) (\sigma_\psi^2 + 2\delta^2) + \frac{|\mathcal{C}^{(r)}|}{|\mathcal{C}|} 4\eta_\phi^3 K_\phi^2 E^2 (E-1) \sigma_\phi^2
\end{aligned} \tag{39}$$

159 The summation of inequality (39) for considering the communication round is given below.

$$\begin{aligned}
& \frac{1}{R} \sum_{r=0}^{R-1} \left(\frac{\eta_\psi E}{8} \mathbb{E}[\tilde{\Delta}_\psi^{(r)}] + \frac{\eta_\phi E |\mathcal{C}^{(r)}|}{|\mathcal{C}|} \mathbb{E}[\Delta_\phi^{(r)}] \right) \\
& \leq \frac{\Delta \mathcal{L}^{(0)}}{R} + 4\eta_\phi^2 K_\phi E^2 \sigma_\phi^2 \left(\frac{|\mathcal{C}^{(r)}|}{|\mathcal{C}|} + \chi^2 \left(1 - \frac{|\mathcal{C}^{(r)}|}{|\mathcal{C}|}\right)\right) + \frac{\eta_\psi^2 K_\psi E^2}{|\mathcal{C}^{(r)}|} \left(\sigma_\psi^2 + 2\delta^2 \left(1 - \frac{|\mathcal{C}^{(r)}|}{|\mathcal{C}|}\right)\right) \\
& \quad + 8\eta_\psi^3 K_\psi^2 E^2 (E-1) (\sigma_\psi^2 + 2\delta^2) + \frac{|\mathcal{C}^{(r)}|}{|\mathcal{C}|} 4\eta_\phi^3 K_\phi^2 E^2 (E-1) \sigma_\phi^2
\end{aligned} \tag{40}$$

160 This is the bound about virtual variable $\tilde{\phi}^{(r+1)}$. To describe this bound with the participants $\phi^{(r+1)}$, the assumption of the
 161 Lipschitz parameter is used as follows.

$$\begin{aligned}
& \mathbb{E} \|\nabla_{\psi} \mathcal{L}(\psi^{(r)}, \phi^{(r)}) - \nabla_{\psi} \mathcal{L}(\psi^{(r)}, \tilde{\phi}^{(r+1)})\|^2 \\
& \leq \frac{1}{|\mathcal{C}|} \sum_{c \in \mathcal{C}} \mathbb{E} \|\nabla_{\psi} \mathcal{L}(\psi^{(r)}, \phi_c^{(r)}) - \nabla_{\psi} \mathcal{L}(\psi^{(r)}, \tilde{\phi}_c^{(r+1)})\|^2 \\
& \leq \frac{\chi^2 K_{\phi} K_{\psi}}{|\mathcal{C}|} \sum_{c \in \mathcal{C}} \mathbb{E} \|\tilde{\phi}_c^{(r+1)} - \phi_c^{(r)}\|^2 \\
& \leq \frac{\chi^2 K_{\phi} K_{\psi}}{|\mathcal{C}|} \sum_{c \in \mathcal{C}} \left(16\eta_{\phi}^2 E^2 \|\nabla_p \mathcal{L}(\psi^{(r)}, \phi_c^{(r)})\|^2 + 8\eta_{\phi}^2 E^2 \sigma_{\phi}^2 \right) = 8\eta_{\phi}^2 E^2 \chi^2 K_{\phi} K_{\psi} \left(\sigma_{\phi}^2 + 2\mathbb{E}[\Delta_{\phi}^{(r)}] \right) \quad (41)
\end{aligned}$$

162 Using the Cauchy–Schwarz inequality described as follows.

$$\|\nabla_{\psi} \mathcal{L}(\psi^{(r)}, \phi^{(r)})\|^2 \leq 2\|\nabla_{\psi} \mathcal{L}(\psi^{(r)}, \phi^{(r)}) - \nabla_{\psi} \mathcal{L}(\psi^{(r)}, \tilde{\phi}^{(r+1)})\|^2 + 2\|\nabla_{\psi} \mathcal{L}(\psi^{(r)}, \tilde{\phi}^{(r+1)})\|^2 \quad (42)$$

163 By utilizing inequality (42), we obtain the following result.

$$\mathbb{E}[\Delta_{\phi}^{(r)}] \leq \mathbb{E}[\tilde{\Delta}_{\psi}^{(r)}] + 16\eta_{\phi}^2 E^2 \chi^2 K_{\phi} K_{\psi} (\sigma_{\phi}^2 + 2\mathbb{E}[\Delta_{\phi}^{(r)}]) \quad (43)$$

164 Through inequality (43), we can get the following inequality.

$$\frac{\eta_{\psi} E}{16} \mathbb{E}[\Delta_{\psi}^{(r)}] + \frac{\eta_{\phi} E |\mathcal{C}^{(r)}|}{32|\mathcal{C}|} \mathbb{E}[\Delta_{\phi}^{(r)}] \leq \frac{\eta_{\psi} E}{8} \mathbb{E}[\tilde{\Delta}_{\psi}^{(r)}] + \frac{\eta_{\phi} E |\mathcal{C}^{(r)}|}{16|\mathcal{C}|} \mathbb{E}[\Delta_{\phi}^{(r)}] + \eta_{\psi} \eta_{\phi}^2 E^3 \sigma_{\phi}^2 \chi^2 K_{\phi} K_{\psi} \quad (44)$$

165 By summing inequality (44) over the total number of communication rounds and applying the parameter settings $\eta_{\phi} =$
166 $\eta/(K_{\phi} E)$ and $\eta_{\psi} = \eta/(K_{\psi} E)$, the proof is completed. \square

167 To ensure that the convergence analysis above remains valid when using an adaptive learning rate in (9), we require
168 that the value of the adaptive learning rate η_c across all clients and rounds is bounded by the same upper bound used in
169 Theorem 12. Since our proposed label shift adaptive learning rate can not have value outside of the bound $[\eta_{min}, \eta_{max}]$ (where
170 $\eta_c^t \in [\eta_{min}, \eta_{max}]$), by appropriately choosing $[\eta_{min}, \eta_{max}] \leq \min \left\{ \frac{1}{24(1+\rho^2)}, \frac{|\mathcal{C}^{(r)}|}{128\chi^2(|\mathcal{C}| - |\mathcal{C}^{(r)}|)}, \sqrt{\frac{|\mathcal{C}^{(r)}|}{\chi^2|\mathcal{C}|}} \right\}$, we guarantee that
171 all learning rates used in the adaptive scheme satisfy the conditions required for Theorem 12.

172 G. Simulation Settings

173 G.1. Datasets

174 We evaluate on various benchmarks including five image-based benchmarks- Tiny ImageNet [32], CIFAR-10 [29], CIFAR-
175 10-C [19], CIFAR-100 [29], and CIFAR-100-C [19], and a text-based benchmark LAMA [50]. The following is a detailed
176 description of the datasets used in this work.

- 177 • **Tiny ImageNet [32]:** Tiny ImageNet is a subset of the ImageNet dataset, containing 200 object classes, each with 500
178 training images, 50 validation images, and 50 test images. All images are RGB and resized to 64×64 pixels.
- 179 • **CIFAR-10 [29]:** The CIFAR-10 dataset consists of 60,000 RGB images of size 32×32 across 10 classes, with 50,000
180 images for training and 10,000 for testing. We applied standard preprocessing including normalization with dataset-wide
181 mean and standard deviation.
- 182 • **CIFAR-10-C [19]:** CIFAR-10-C is an extension of the CIFAR-10 dataset designed to evaluate model robustness against
183 common corruptions. It contains 950,000 images created by applying 19 different types of corruption—such as noise, blur,
184 weather effects, and digital distortions—at 5 severity levels to the original CIFAR-10 test set of 10,000 images.
- 185 • **CIFAR-100 [29]:** CIFAR-100 is a fine-grained variant of CIFAR-10 containing 100 object classes. It consists of 60,000
186 color images at 32×32 pixels, split into 50,000 training and 10,000 test images. The 100 classes are grouped into 20
187 superclasses for hierarchical classification research.
- 188 • **CIFAR-100-C [19]:** CIFAR-100C applies the same 19 corruption types with 5 severity levels from CIFAR-10-C onto
189 the CIFAR-100 dataset. It consists of 950,000 corrupted images used as a benchmark for analyzing model robustness on
190 fine-grained image classification tasks.
- 191 • **LAMA [50]:** LLanguage Model Analysis is a benchmark dataset designed to evaluate the factual and commonsense
192 knowledge acquired by language models. In our experiments, we focus on the T-REx subset of LAMA, which consists
193 of (subject, relation, object) triples derived from Wikidata. This subset consists of 41 relational tasks, with 100 samples
194 randomly sampled per task. To simulate heterogeneous client environments, we assign disjoint subsets of tasks to different
195 clients.

196 G.2. Online Distribution Shift Modeling

197 To emulate online distribution shift in (1), each client’s data distribution moves from a common initial uniform vector \mathbf{Q}_c^0
198 toward a client-specific target \mathbf{Q}_c^T according to a time-dependent weight $\omega(t)$. We evaluate under four prototypical distribution
199 shift schedules—linear (Lin.), sine (Sin.), square (Squ.), and Bernoulli (Ber.), each driving a client’s distribution from a
200 uniform start toward a client-specific target [10, 45, 56, 65, 69]. Following is a detailed description of four prototypical
201 label-shift schedules according to different $\omega(t)$ functions, and Figure 3 shows how the parameter $\omega(t)$ changes over time for
202 various shift types.

- 203 • **Linear shift (Lin.):** $\omega(t) = \frac{t}{T}$, where t is the current timestep and T is the total number of timesteps. This provides a smooth
204 and gradual transition from \mathbf{Q}_c^0 to \mathbf{Q}_c^T over time.
- 205 • **Sine shift (Sin.):** $\omega(t) = \sin\left(\frac{\pi t}{\sqrt{T}}\right)$. This introduces cyclical variations, capturing periodic shifts in the data distribution.
- 206 • **Square Shift (Squ.):** $\omega(t)$ alternates between 0 and 1 every $\frac{\sqrt{T}}{2}$ timestep, resulting in abrupt, periodic changes in the class
207 distribution.
- 208 • **Bernoulli shift (Bern.):** $\omega(t)$ retains its previous value $\omega(t-1)$ with a probability of $\frac{1}{\sqrt{T}}$, or flips to $1 - \omega(t-1)$.
209 This configuration captures stochastic variations, ensuring that class priors change randomly while maintaining a scale
210 proportional to \sqrt{T} .

211 For \mathbf{Q}_c^T , we used the Dirichlet distribution to consider heterogeneous data distributions among clients. The distribution
212 factor α of the Dirichlet distribution controls the level of heterogeneity among clients. Smaller α leads more heterogeneous
213 distribution, and Larger α leads to Independent and identically distributed data system. In this study, we set $Dir(\alpha = 0.1)$.
214 Figure 4 visualizes the heterogeneity among clients according to Dirichlet distribution factor α .

215 G.3. Distribution Shift Scenarios

216 In all experiments, each target distribution of client \mathbf{Q}_{y^T} in (1) is defined according to the specific type of distribution shift
217 being simulated. We summarize below the construction and datasets used for each shift scenario.

- 218 • **Label Shift.** Label shift simulations are conducted on Tiny ImageNet [32], CIFAR-10 [29], and LAMA [50], where each
219 client’s class prior evolves over time according to one of four temporal schedules (Lin., Sin, Squ., Ber.) which follows (1).
- 220 • **Covariate Shift.** The target feature distribution $\mathbf{Q}_{c,x}^T$ reflects corruption-induced changes to the input domain. Each

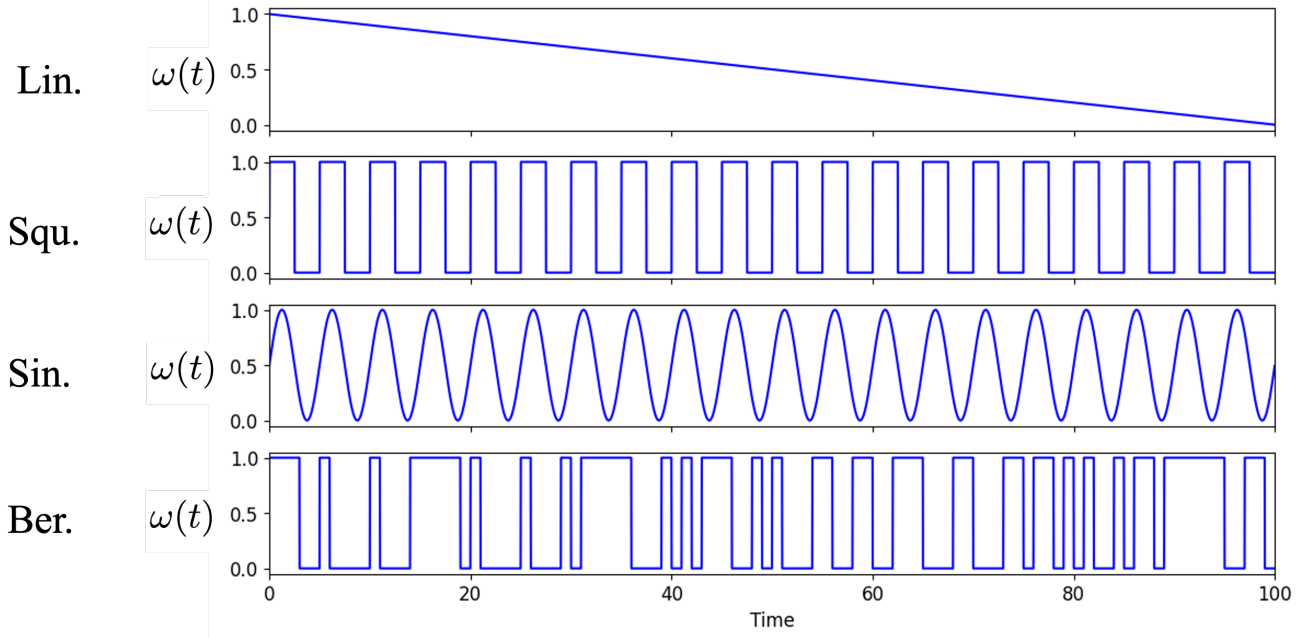


Figure 3. Visualization of how the parameter $\omega(t)$ changes over time for various shift types. The Lin. presents a steady and continuous increase or decrease, reflecting a gradual and predictable change. Both the Squ. and Sin. display periodic patterns. The Squ. alternates sharply between two values at regular intervals, while the Sin. oscillates smoothly in a wave-like manner. The Ber. introduces randomness at each timestep, resulting in a stochastic and less predictable trajectory for $\omega(t)$.

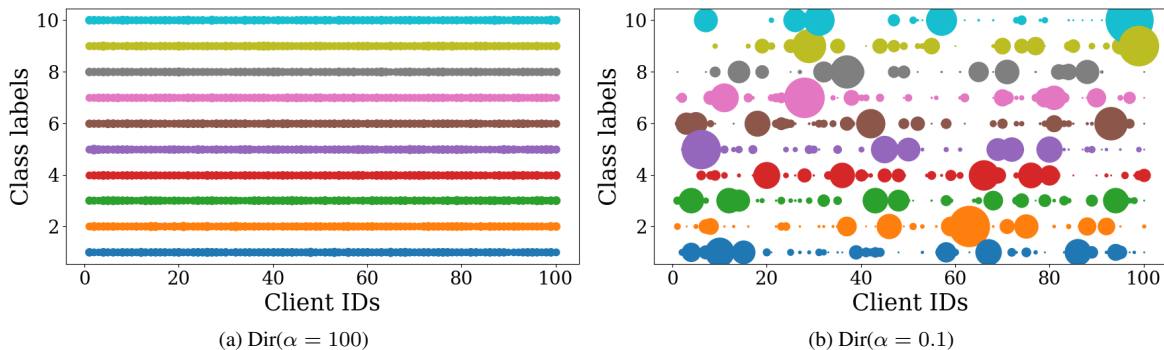


Figure 4. Visualization of heterogeneity among clients according to Dirichlet distribution factor α in CIFAR-10 dataset. The x -axis represents the ID of the client, while the y -axis represents the class of the data. The color of the circles varies with each class type, and the size of the circles indicates the size of the data. This level of heterogeneity is not dependent on the data set but on α values.

221 client is assigned a distinct and fixed corruption type (e.g., Gaussian noise, blur), while the corruption severity level shifts
 222 dynamically over time according to one of four temporal schedules. We use the CIFAR-10 [29] \rightarrow CIFAR-10-C [19] and
 223 CIFAR-100 [29] \rightarrow CIFAR-100-C [19] benchmarks to simulate these covariate-shift environments.

224 G.4. Compared Methods

225 We evaluate our proposed Fed-ADE against six existing unsupervised online adaptation baselines:

- 226 • **FTH** [58]: FTH maintains an average of estimated label distributions across all previous timesteps. By aggregating the
 227 entire history of predictions, FTH assumes that past distributional information is informative for current adaptation, making
 228 it robust to gradual, monotonic shifts but potentially less responsive to abrupt changes.
- 229 • **ATLAS** [2]: ATLAS maintains an ensemble of base learners, each optimized with a distinct learning rate. Using an
 230 exponential weighting scheme, ATLAS dynamically aggregates these learners according to their recent performance,

- 231 enabling robust adaptation to various patterns and magnitudes of label shift.
- 232 • **UDA [18]**: UDA is a technique where a model is trained on labeled data from a source domain and adapted to work well
- 233 on a target domain that has no labels, even though the data distributions are different. The main idea is to reduce the gap
- 234 between the source and target domains by aligning their feature representations or adjusting the model so it can generalize to
- 235 the target data, all without using any target domain labels.
- 236 • **UNIDA [63]**: UNiDA is a method designed to handle domain adaptation scenarios. This assumes the same class set across
- 237 domains, which aims to adapt models by distinguishing between common, source-private, and target-private classes, often
- 238 using prototype-based or confidence-based techniques to avoid misclassifying unknown target classes as known ones.
- 239 • **Fed-POE [43]**: Fed-POE is a federated online adaptation framework in which each client combines local fine-tuning with
- 240 an ensemble of periodically aggregated global models. While this approach supports client personalization and leverages
- 241 federated knowledge, it employs a fixed learning rate and incurs computational overhead from managing multiple model
- 242 instances.
- 243 • **FedCCFA [9]**: FedCCFA is a federated learning framework for concept shift, where clients may experience different
- 244 distributions. It performs class-level classifier clustering to share aggregated class-wise classifiers among similar clients, and
- 245 aligns feature spaces using clustered feature anchors with an entropy-based adaptive weighting.

246 G.5. Hyperparameters

247 In this section, we summarize hyperparameters used in the simulations.

Table 6. Hyperparameters for Tiny ImageNet, CIFAR-10, and CIFAR-100.

Hyperparameter	Tiny ImageNet	CIFAR-10	CIFAR-100
Number of clients	100	100	100
Communication rounds (R)	10	10	10
Local epochs	4	4	4
Optimizer	SGD	SGD	SGD
Batch size	128	32	32
Participant rate	10%	10%	10%
Model architecture	ResNet18	CNN w/ 3 residual blocks	CNN w/ 3 residual blocks
Shared layers (ψ_c)	Representation layers	Representation layers	Representation layers
Lowest learning rate	5×10^{-6}	5×10^{-6}	5×10^{-6}
Highest learning rate	10^{-4}	10^{-4}	10^{-4}

Table 7. Hyperparameters for CIFAR-10-C, CIFAR-100-C, and LAMA

Hyperparameter	CIFAR-10-C	CIFAR-100-C	LAMA
Number of clients	100	100	5
Communication rounds (R)	10	10	5
Local epochs	4	4	1
Optimizer	SGD	SGD	AdamW
Batch size	32	32	4
Participant rate	10%	10%	100%
Model architecture	CNN w/ 3 residual blocks	CNN w/ 3 residual blocks	Llama-3.2-3B
Shared layers (ψ_c)	Representation layers	Representation layers	LoRA on q/k/v (layers 0-13)
Lowest learning rate	5×10^{-6}	5×10^{-6}	1×10^{-3}
Highest learning rate	1×10^{-4}	1×10^{-4}	1×10^{-2}

248 G.6. Hardware Specifications

Table 8. Hardware specifications used for all simulations.

Component	Specification
CPU	AMD Ryzen 9 7950X, 16-Core, 32 Threads
GPU	NVIDIA GeForce RTX 3090X2
RAM	256 GB DDR5
Storage	1.8 TB NVMe SSD

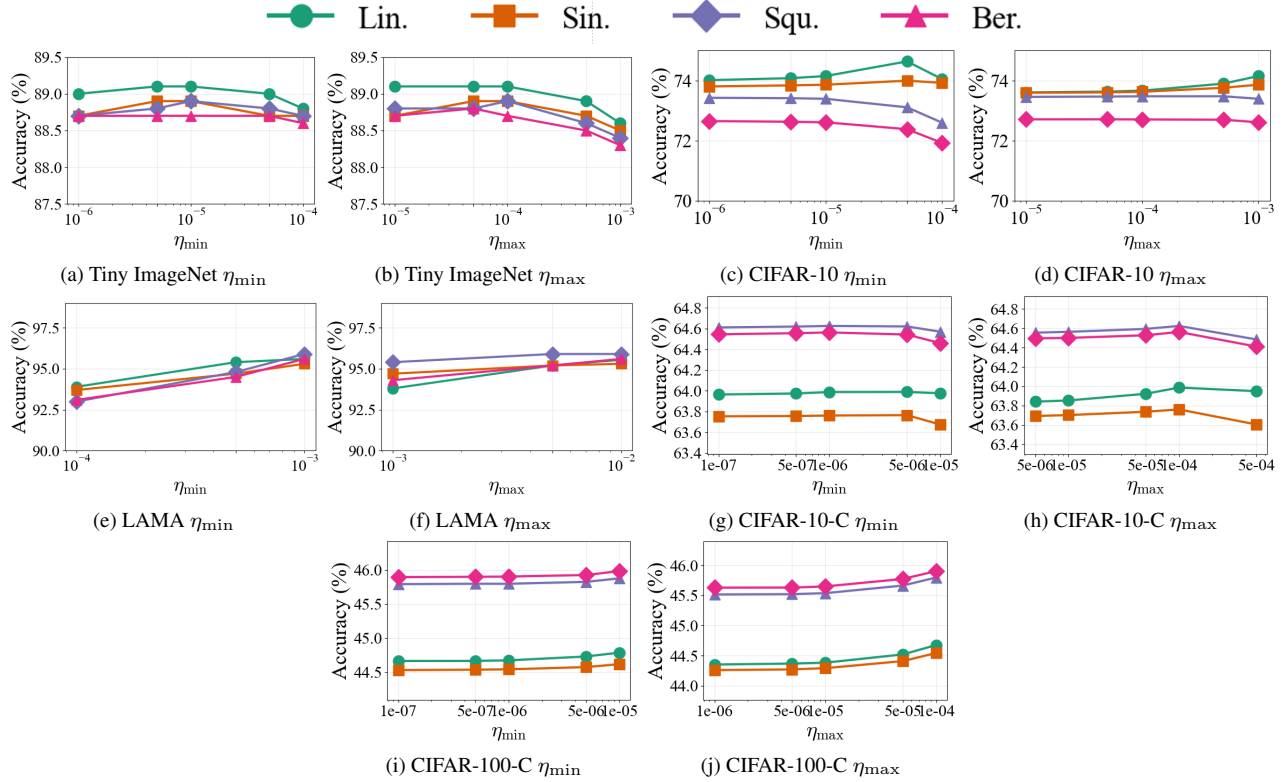


Figure 5. Impact of learning rate bounds on Fed-ADE under label shift scenarios.

249 H. Extra Simulation Results

250 H.1. Impact of Learning Rate Selection

251 Figure 5 examines the sensitivity of Fed-ADE to the choice of learning rate bounds under all scenarios and benchmarks.
 252 For image benchmarks, we vary η_{\min} while fixing $\eta_{\max} = 10^{-4}$, and vary η_{\max} while fixing $\eta_{\min} = 5 \times 10^{-6}$. For text
 253 benchmark LAMA, we vary η_{\min} while fixing $\eta_{\max} = 10^{-2}$, and vary η_{\max} while fixing $\eta_{\min} = 10^{-4}$. Across all cases,
 254 Fed-ADE consistently maintains high accuracy within a broad range of hyperparameter choices. While extreme values lead to
 255 slight performance degradation, the overall trend shows that our dynamics-driven adaptation is far less sensitive to the exact
 256 learning rate bounds compared to fixed-rate baselines. This robustness highlights that Fed-ADE reduces the need for extensive
 257 hyperparameter tuning, an essential property in federated and online learning where search budgets are limited.

Table 9. Performance comparison of different online distribution shift adaptation methods across datasets and shift types with pretrained model from Gaussian distribution (average accuracy (%) and average wall time (sec.))

Dataset	Shift	Localized Learning				Federated Learning					Fed-ADE
		FTH	ATLAS	UNIDA	UDA	Fed-POE	FedCCFA	FixLR(Low)	FixLR(Mid)	FixLR(High)	
(i) Label Shift Scenarios											
Tiny ImageNet	Lin.	74.1±2.3	70.7±2.1	75.1±2.1	63.1±2.3	81.5±1.2	81.7±1.8	81.5±1.1	81.2±1.3	78.1±1.5	84.5±1.1
	Sin.	73.7±2.4	71.1±1.9	74.8±2.5	61.3±2.1	82.1±1.2	80.9±1.1	81.9±1.7	81.0±2.1	77.5±2.1	84.7±0.7
	Squ.	72.6±2.4	70.9±1.8	74.6±2.2	61.7±2.1	81.5±1.3	78.8±1.9	82.4±1.2	80.9±1.6	77.7±1.3	83.9±0.9
	Ber.	72.1±2.3	71.0±2.0	74.7±2.1	61.1±1.7	80.9±1.6	79.1±1.1	82.1±0.9	80.8±1.7	77.8±1.5	84.2±0.4
CIFAR-10	Lin.	28.4±1.7	22.6±3.3	17.2±4.1	27.4±4.2	66.1±1.2	53.6±2.1	64.8±2.2	65.7±2.1	51.3±3.1	68.0±1.7
	Sin.	28.9±2.1	23.1±3.1	18.3±4.5	27.1±3.7	66.7±1.2	53.3±2.1	64.7±1.9	65.1±1.8	51.6±4.1	67.7±1.7
	Squ.	25.9±1.7	21.6±2.6	15.8±3.7	25.1±2.2	67.1±1.5	54.3±1.3	64.8±1.2	65.7±1.6	52.3±3.5	66.4±1.6
	Ber.	26.1±2.1	21.7±2.9	16.1±4.1	24.5±2.5	67.0±1.3	54.1±1.3	64.3±1.7	65.4±1.4	52.6±2.8	67.1±1.3
(ii) Covariate Shift Scenarios											
CIFAR-10	Lin.	15.4±0.4	10.1±0.8	39.1±0.5	37.8±1.1	41.6±0.4	35.2±0.5	58.0±0.6	58.1±0.6	36.7±2.4	59.5±0.5
	Sin.	15.2±0.5	11.9±0.7	39.2±0.4	37.2±0.9	41.7±0.6	33.1±0.4	57.1±0.5	57.8±0.7	35.3±1.7	59.3±0.5
CIFAR-10-C	Squ.	13.5±0.5	13.1±0.6	38.3±0.4	36.8±1.2	43.1±0.5	32.1±0.7	56.9±0.9	57.3±1.1	35.6±2.1	60.4±0.5
	Ber.	14.8±0.5	12.2±1.1	38.7±0.4	36.6±1.1	43.2±0.5	33.0±0.5	56.7±0.7	67.1±1.0	46.1±2.7	60.3±0.4
CIFAR-100	Lin.	4.2±1.7	2.4±0.2	29.1±0.1	31.3±0.3	20.2±0.4	20.7±0.6	42.0±0.4	40.8±0.2	37.1±1.1	43.1±0.5
	Sin.	5.6±2.2	2.5±0.1	29.5±0.3	30.7±0.8	20.3±0.5	20.7±0.6	41.9±0.4	40.9±0.3	36.6±1.3	44.4±0.4
CIFAR-100-C	Squ.	5.7±2.1	3.2±0.3	27.1±0.4	29.1±0.7	22.9±0.4	18.6±0.8	41.6±0.3	41.2±0.5	37.1±1.5	45.1±0.5
	Ber.	6.1±1.8	3.1±0.4	27.8±0.4	29.6±0.8	21.8±0.8	19.3±0.8	40.3±0.5	41.4±0.5	34.1±1.4	44.8±0.6

258 H.2. Impact of Distribution of Pre-training Data

259 In practical federated deployments, the exact distribution of the pre-training data on the server is often unknown to clients.
 260 To examine the robustness of Fed-ADE under such realistic conditions, we evaluate post-adaptation performance on image
 261 benchmarks when the pre-training data follows two non-uniform distributions: *Gaussian* and *Exponential Decay*. As shown in
 262 Table 9, and Table 10, Fed-ADE maintains consistently strong performance across all distribution settings and shift types,
 263 with only a minor variation compared to the uniform case (cf. Table 1). These results demonstrate that our dynamics-based
 264 adaptation effectively generalizes even when the pre-training distribution differs from the assumed prior, validating its
 265 robustness under practical deployment scenarios.

266 H.3. Why Cosine Similarity? Alternatives and Ablations

267 In this paper, our Fed-ADE must be (i) online & per-client (no extra communication), (ii) label-free (only pseudo-
 268 labels/representations), (iii) robust to pseudo-label noise and transient shifts, (iv) lightweight in compute and memory,
 269 and (v) bounded and interpretable so that we can stably map it to a learning rate in $[\eta_{\min}, \eta_{\max}]$ across heterogeneous clients.

270 Cosine similarity meets these requirements

- 271 • **Bounded:** S_c^t is bounded in $[0, 1]$, so it leads to a stable mapping to learning across clients and timestep
- 272 • **Efficient:** Linear-time, no optimization/probabilistic inference
- 273 • **Robust:** Scale-invariant and less sensitive to sparsity/outliers in pseudo-label histograms; temperature rescaling or mild
 274 miscalibration does not change directions.

275 **Alternatives considered** We implemented three commonly suggested alternatives and found consistent drawbacks in our
 276 setting.

277 **(1) KL divergence on batch histograms:** *Pros:* classical information-theoretic distance. *Cons:* asymmetric and *un-*
 278 *bounded;* becomes unstable/infinite under zeros/sparsity—common with noisy pseudo-labels on small batches. Requires
 279 smoothing/regularization and hyperparameters (e.g., ϵ -floor), which are highly dataset/client dependent and harm cross-client
 280 consistency. Mapping an unbounded statistic to a stable learning rate is delicate.

281 **(2) Wasserstein distance:** Requires a ground metric on classes or high-dim features; even with Sinkhorn regularization, it
 282 needs iterative optimization (per batch pair) and careful tuning. *Pros:* captures geometric discrepancies. *Cons:* higher compute

Table 10. Performance comparison of different online distribution shift adaptation methods across datasets and shift types with pretrained model from exponential decay distribution(average accuracy (%) and average wall time (sec.))

Dataset	Shift	Localized Learning				Federated Learning					Fed-ADE
		FTH	ATLAS	UNIDA	UDA	Fed-POE	FedCCFA	FixLR(Low)	FixLR(Mid)	FixLR(High)	
(i) Label Shift Scenarios											
Tiny ImageNet	Lin.	78.2±1.0	70.2±2.1	77.3±0.8	69.0±0.6	79.9±0.3	82.1±0.4	81.8±0.5	82.5±0.3	81.4±0.2	83.1±0.4
	Sin.	77.9±0.8	71.4±1.6	77.1±0.6	69.4±0.5	80.4±0.6	81.5±0.4	82.1±0.2	82.7±0.5	81.3±0.3	82.7±0.5
	Squ.	77.2±0.8	71.1±1.8	76.9±0.6	69.4±0.5	80.9±0.5	81.2±0.3	82.3±0.4	82.1±0.4	80.1±0.3	82.6±0.3
	Ber.	78.2±1.1	70.7±1.6	76.6±0.7	69.7±0.4	80.4±0.5	80.4±0.3	81.1±0.4	82.1±0.2	80.4±0.3	81.8±0.4
CIFAR-10	Lin.	27.7±1.4	29.0±2.0	20.2±1.3	27.6±1.8	65.1±1.0	63.8±0.9	64.1±1.4	64.8±1.3	60.1±1.3	66.2±1.7
	Sin.	28.4±1.2	28.3±2.0	20.3±1.1	28.1±1.6	64.7±0.6	63.1±1.3	63.8±1.2	64.3±1.4	60.3±0.8	65.9±1.7
	Squ.	27.1±1.2	28.5±1.8	21.1±0.9	24.8±1.6	64.6±0.9	62.8±1.1	64.5±1.1	64.1±1.6	61.1±0.9	66.4±1.5
	Ber.	26.6±1.5	27.1±1.9	20.7±1.1	25.1±2.1	64.3±1.1	62.3±0.7	64.7±1.4	63.8±1.5	60.8±1.2	67.1±1.3
(ii) Covariate Shift Scenarios											
CIFAR-10	Lin.	23.7±0.2	13.9±0.2	43.3±0.6	45.7±0.8	44.5±0.8	43.1±0.5	63.4±0.2	63.9±0.3	40.6±2.1	58.3±0.5
	Sin.	22.9±0.2	13.2±0.2	44.8±0.1	43.5±0.3	44.7±1.2	43.3±0.4	63.5±0.3	63.7±0.3	38.1±3.1	58.2±0.5
CIFAR-10-C	Squ.	23.8±0.1	14.1±0.4	42.2±0.1	43.3±0.2	48.5±1.2	41.6±0.7	62.7±2.1	64.5±2.1	39.6±2.8	59.0±0.5
	Ber.	23.6±0.2	14.2±0.3	42.7±0.2	42.3±0.1	48.7±0.9	42.0±0.5	64.1±2.1	64.4±2.1	40.8±2.2	59.0±0.4
CIFAR-100	Lin.	5.1±1.8	6.4±0.4	24.4±0.5	27.6±0.5	19.1±2.1	17.9±1.1	40.8±0.5	39.1±0.6	37.7±1.2	42.7±0.5
	Sin.	5.3±1.7	5.1±0.4	24.3±0.6	28.1±0.5	20.1±1.9	18.3±1.1	40.7±0.6	38.6±0.7	37.6±1.2	42.4±0.6
CIFAR-100-C	Squ.	4.8±1.5	4.7±0.5	24.1±0.4	28.3±0.7	19.8±2.1	18.1±0.9	39.4±0.6	38.2±0.7	38.1±1.1	42.1±0.4
	Ber.	4.3±1.3	5.1±0.3	23.5±0.4	27.8±0.6	19.7±2.3	16.9±1.0	40.1±0.4	37.7±0.6	37.8±1.2	42.0±0.5

and memory; sensitive to transient fluctuations; scale depends on ground metric \Rightarrow learning rate scaling across clients becomes ill-conditioned. In high-dim feature space, pairwise costs/transport exacerbate overhead.

(3) Bayesian change-point detection: *Pros:* probabilistic treatment of regime switches. *Cons:* assumes i.i.d. within segments and requires prior modeling; posterior updates/inference add computation; fragile to batch-level noise (false alarms/delays). Typically designed for detection (binary), not for per-step *continuous* shift magnitudes needed to drive learning rate.

Performance comparison of cosine similarity vs. alternatives We compared cosine similarity with KL, Wasserstein, and Bayesian CPD under four dynamic shift patterns (Lin./Sin./Squ./Ber.) on CIFAR-10. Cosine consistently achieved the best accuracy:

Measure	Lin.	Sin.	Squ.	Ber.
Fed-ADE (Cosine similarity)	73.8 ± 0.6	73.6 ± 0.5	72.2 ± 1.6	72.9 ± 2.2
KL divergence	63.2 ± 3.8	62.4 ± 2.3	61.1 ± 3.4	61.4 ± 3.6
Wasserstein	70.8 ± 0.6	69.9 ± 1.1	68.8 ± 1.3	66.5 ± 2.1
Bayesian CPD	71.5 ± 0.5	70.8 ± 0.8	69.7 ± 2.4	69.0 ± 1.1

Gains of the cosine similarity method are largest under label noise and transient shifts, where bounded, direction-only comparison stabilizes learning rate scaling across clients.